Monthly Notices
of the
ROYAL ASTRONOMICAL SOCIETY

Mon. Not. R. Astron. Soc. **416,** 1118–1134 (2011) doi:10.1111/j.1365-2966.2011.19110.x

Weakening dark matter cusps by clumpy baryonic infall

David R. Cole,★ Walter Dehnen★ and Mark I. Wilkinson★

Theoretical Astrophysics Group, Department of Physics & Astronomy, University of Leicester, Leicester LE1 7RH

Accepted 2011 May 19. Received 2011 May 18; in original form 2011 February 9

ABSTRACT

We consider the infall of a massive clump into a dark matter halo as a simple and extreme model for the effect of baryonic physics (neglected in gravity-only simulations of large-scale structure formation) on the dark matter. We find that such an infalling clump is extremely efficient in altering the structure of the halo and reducing its central density: a clump of 1 per cent the mass of the halo can remove about twice its own mass from the inner halo and transform a cusp into a core or weaker cusp. If the clump is subsequently removed, mimicking a galactic wind, the central halo density is further reduced and the mass removed from the inner halo doubled. Lighter clumps are even more efficient: the ratio of removed mass to clump mass increases slightly towards smaller clump masses. This process becomes more efficient the more radially anisotropic the initial dark matter velocities are. While such a clumpy infall may be somewhat unrealistic, it demonstrates that the baryons need to transfer only a small fraction of their initial energy to the dark matter via dynamical friction to explain the discrepancy between predicted dark matter density profiles and those inferred from observations of dark-matter-dominated galaxies.

Key words: galaxies: formation – galaxies: haloes – galaxies: kinematics and dynamics – galaxies: structure.

1 INTRODUCTION

The success of the lambda cold dark matter (ΛCDM) paradigm of cosmological structure formation in reproducing the observed structure of the Universe on scales $\gtrsim$1 Mpc is now well-established (see e.g. Springel, Frenk & White 2006, and references therein). However, on the scale of individual galaxies ($\lesssim$100 kpc) the density profiles of dark matter haloes pose a potentially significant problem. The form of these profiles in the absence of baryonic physics has been extensively studied by means of numerical simulations. Dubinski & Carlberg (1991) and Navarro, Frenk & White (1997), NFW, showed that haloes on a range of mass scales have similar profiles, with the density in the innermost regions exhibiting a $\rho \propto r^{-1}$ cusp. More recent work has found that the haloes can be better represented by profiles with either slightly shallower inner cusp slopes (Dehnen & McLaughlin 2005; Navarro et al. 2010) or continuously varying slope, for example the Einasto & Einasto (1972) profile (Navarro et al. 2004).

However, there is mounting observational evidence that galaxies occupy dark matter haloes with almost uniform density cores with the strongest evidence coming from low surface brightness galaxies (see de Blok 2010, for a recent review). Although there have been fewer such studies in high surface brightness spirals, recent work by Spano et al. (2008) has shown that in these galaxies also cored haloes are favoured. Even in low-luminosity, pressure-supported systems such as the dwarf spheroidal satellite galaxies surrounding the Milky Way, there is circumstantial evidence that their haloes are not cusped (Gilmore et al. 2007).

It is important to remember, however, that the ignorance of baryonic physics in the aforementioned simulations constitutes a significant limitation with regard to any discussion of the inner halo profiles. The inclusion of baryon physics is widely recognized as a crucial, albeit extremely technically challenging prerequisite for further progress in understanding galaxy formation.

There are multiple ways in which the baryons can affect the density profile of a dark matter halo. First, a cloud of gas which initially extends throughout a cusped dark matter halo can dissipate energy by radiation and contract to the centre of the halo. As the dark matter responds to the deeper gravitational potential, this in turn leads to a steepening of the dark matter cusp, known as adiabatic contraction (Blumenthal et al. 1986). This is not necessarily the end of the story, however, as baryons also have the ability to generate mass outflows driven by stellar winds and supernovae produced as a result of star formation. Depending on the efficiency of star formation, such processes can expel a significant fraction of the baryonic mass from the central regions of a galaxy, resulting in a large-scale rearrangement of the dark matter. Using semi-analytic arguments, Gnedin & Zhao (2002) found that when stellar mass loss was preceded by adiabatic

---

★E-mail: david.cole@astro.le.ac.uk (DRC); walter.dehnen@astro.le.ac.uk (WD); mark.wilkinson@astro.le.ac.uk (MIW) contraction, the resulting halo distribution was almost unchanged from its original cusped profile. Read & Gilmore (2005), however, subsequently showed that repeated episodes of adiabatic contraction followed by rapid mass expulsion could give rise to a reduction in the central density and hence produce cored haloes. This occurs because although the initial infall/outflow produces the same mass density profile, the velocity structure of the dark matter halo after the outflow is biased towards radial orbits. As a result, subsequent events are able to lower the inner density more easily.

Another way in which the baryonic component of a galaxy can transfer energy to the dark matter halo is by means of a stellar bar. Weinberg & Katz (2002) proposed that the rotation of bars is decelerated by the exchange of energy and angular momentum with dark matter particles on orbits in resonance with the bar's rotation. While further work by Athanassoula (2002, 2003) confirmed this conclusion, the size required for a stellar bar to significantly change the mass distribution in the inner regions of a dark matter halo was found to be much larger than those observed in barred galaxies. Hence, this mechanism is thought to be of limited importance for the majority of dark matter haloes, though the deceleration process is certainly affecting the evolution of galactic bars.

However, galaxy formation also involves violent processes, where baryonic inflow is neither smooth nor adiabatic. Gas accretion is likely to occur during galaxy mergers, when it takes the form of clumpy infall rather than the slow contraction of a smooth cloud. Although a baryon clump falling into the centre of a dark halo will add to the gravitational potential there (and thus increase the binding energy of the dark halo), it can, during this process, lose its orbital energy via dynamical friction. El-Zant, Shlosman & Hoffman (2001) showed that the energy thus gained (i.e. binding energy lost) by the dark matter can produce an observable impact on the dark matter density profile. El-Zant et al. (2004) and Nipoti et al. (2004) extended this work by performing *N*-body simulations of galaxy clusters, where the infalling galaxies play the role of clumps. They found that the initial dark matter cusp can be softened through the transfer of energy from the baryonic clumps to the dark matter though the overall density profile, including the baryonic component, remained cusped.

Attempts have also been made to add full baryonic physics to the studies of sinking clumps mainly based on the results of cosmological simulations, which try to model the effect of cooling, metal enrichment and supernova feedback (e.g. Gnedin et al. 2004; Romano-Díaz et al. 2008; Johansson, Naab & Ostriker 2009; Pedrosa, Tissera & Scannapieco 2009). These simulations confirmed the transfer of energy and angular momentum from baryons to the dark matter, while the results on the dark matter density reduction were conflicting. This is presumably because of varying amounts, depending on the details of the respective model, of contraction owed to the additional gravitational pull from the accreted baryons.

Despite these promising attempts, a truly realistic modelling of baryonic physics is still beyond contemporary simulation techniques, not least because important baryonic processes, such as re-ionization as well as primordial and ordinary star formation, are themselves not sufficiently understood. Therefore, it is important to understand more quantitatively the purely stellar dynamical aspect of this mechanism, which alone affects the dark matter distribution. Some progress towards this goal has been made recently by Jardel & Sellwood (2009) and Goerdt et al. (2010). However, a complete understanding of the pure stellar dynamical problem is still missing, but seems essential before attempting to interpret the results of simulations which include baryons. In the present paper, we build on this previous work to explore the impact of clumpy baryonic infall more broadly. We consider more realistic initial conditions. In particular, we focus on clumps initially on parabolic orbits, which may become bound to a halo during a merger event, and haloes with anisotropic velocity distributions, the expected situation to obtain within the hierarchical structure formation scenario of CDM.

The outline of the paper is as follows. In Section 2 we consider analytical estimates for the damage done to the halo by the energy transfer from the satellite orbit. Section 3 gives our modelling approach for the *N*-body simulations, while Sections 4 and 5 describe the resulting orbital decay and typical changes induced in the simulated haloes. Sections 6 and 7 discuss the effect of halo velocity anisotropy on both orbital decay and damage to the halo, while Section 8 considers the effect of satellite mass and size. In Section 9 we demonstrate the effect of removing the accreted clump, corresponding to a galactic wind subsequent. Finally, Sections 10 and 11 summarize and discuss our findings, respectively.

2 THEORETICAL ARGUMENTS

Chandrasekhar's (1943) dynamical friction formula for systems with a Maxwellian velocity distribution of dispersion σ (equation 8.7 of Binney & Tremaine 2008),

$$\frac{\mathrm{d}\boldsymbol{v}_\mathrm{s}}{\mathrm{d}t} \simeq -\hat{\boldsymbol{v}}_\mathrm{s}\,\frac{4\pi G^2 m_\mathrm{s}\,\rho\ln\Lambda}{v_\mathrm{s}^2}\left[\mathrm{erf}(x) - \frac{2x}{\sqrt{\pi}}\mathrm{e}^{-x^2}\right]_{x=v_\mathrm{s}/\sqrt{2}\sigma} \qquad (1)$$

($\ln\Lambda$ is the Coulomb logarithm, m_s and $\boldsymbol{v}_\mathrm{s}$ are the mass and velocity of the clump or satellite and ρ is the mass density of dark matter particles), shows that the deceleration is proportional to m_s, such that the time for the orbit to decay $t_\mathrm{infall} \propto m_\mathrm{s}^{-1}$. In particular, for this orbital decay to occur within (less than) a Hubble time, a mass of $m_\mathrm{s} \sim 10^{6-8}\,\mathrm{M}_\odot$, depending on the size of the dark matter halo, is required. Chandrasekhar's formula also suggests that the drag force is strongest for small v_s (because this increases the interaction time between perturber and dark matter particles) and/or for large ρ.

However, the formula cannot be used to assess the effect the infalling clump has on the dark matter. A simple estimate for the mass removed from the inner parts of the dark matter halo can be obtained from the following argument originally due to Goerdt et al. (2010, preprint version). Assuming a circular orbit for the perturber, the specific energy lost when sinking from radius $r + \delta r$ to r is

$$\delta\varepsilon_\mathrm{s} = \frac{\mathrm{d}}{\mathrm{d}r}\left[\frac{GM(r)}{2r} + \Phi(r)\right]\delta r = 2\pi G\,r\left(\frac{\bar\rho}{3} + \rho\right)\delta r, \qquad (2)$$

with $\bar\rho(r)$ the mean density interior to radius r. Assuming this energy is injected into the spherical shell at radius r, each dark matter particle at that radius gains specific energy $(\delta\varepsilon_\mathrm{s}/\delta r)(m_\mathrm{s}/4\pi\rho r^2)$. A density core forms and the sinking of the clump stalls (Read et al. 2006) as soon as this energy equals the specific kinetic energy of each particle, which may be estimated as $v_\mathrm{circ}^2/2 = GM(r)/2r$. With equation (2), this yields (with $\gamma = -\mathrm{d}\ln\rho/\mathrm{d}\ln r$)

$$M(r) \sim \left[1 + \frac{\bar\rho(r)}{3\rho(r)}\right] m_\mathrm{s} \simeq \frac{4-\gamma}{3-\gamma}\,m_\mathrm{s}. \qquad (3)$$

This argument suggests (i) that the mass ejected by the perturber is comparable to its own mass, and (ii) that the density core which forms in response to the heating induced by the sinking baryonic clump has radius comparable to that at which the originally enclosed mass equals m_s.

Strictly speaking, this argument only applies to circular orbits, which are not very realistic, and the assessment of the heating required to turn a cusp into a core is rather crude. We now present

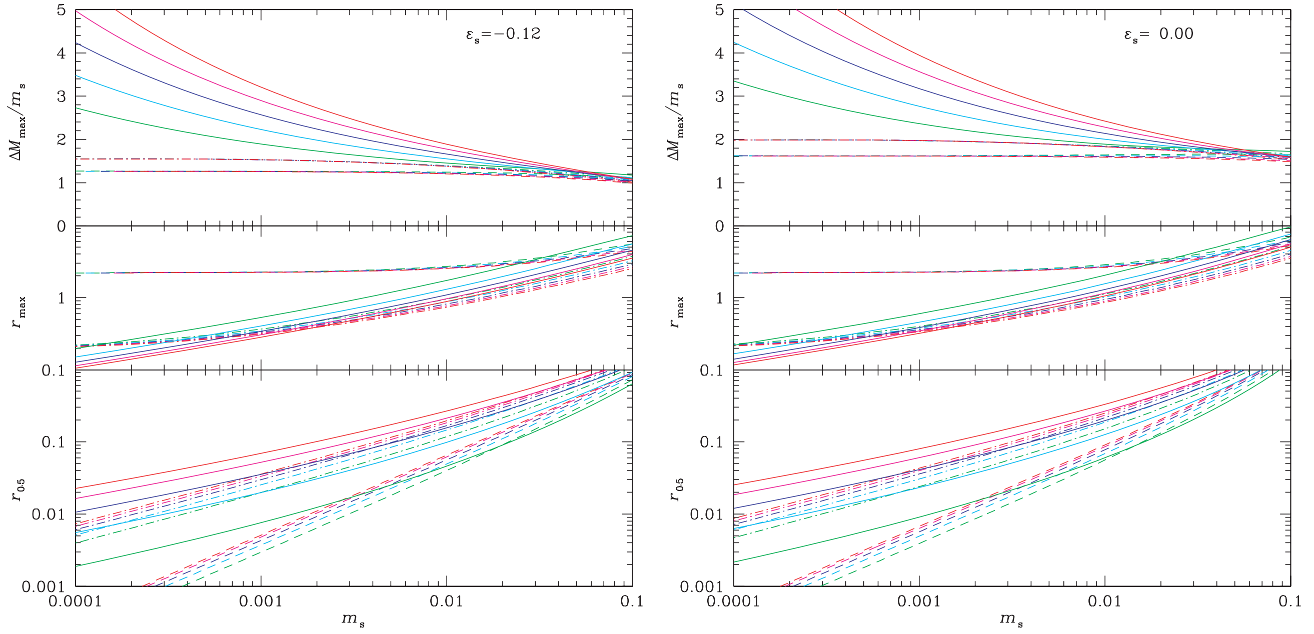

Figure 1. Predictions, using equation (8), for the ratio of the maximum excavated mass to the mass of the infalling clump (top), the radius at which this occurs (middle) and the radius inside of which half the mass has been removed (bottom; in units of halo scale radius) as function of the mass of the accreted clump. The clump was assumed to be initially either on a bound orbit with energy equal to that of the circular orbit at halo half-mass radius (left) or on a parabolic orbit (right). The initial halo is modelled to have density distribution (12) also used in our simulations, while for the final halo we used the models of equation (11) (solid) or equation (10) (dashed: $\eta = 0.9$ or dash–dotted: $\eta = 1.5$). The different lines correspond to inner density slopes for the final halo between $\gamma_0 = 0$ (red) and $\gamma_0 = 0.4$ (green), while along each line the scale radii r_0 of the final model are varied (and m_s obtained from equation 8).

a more quantitative estimate based on the exact energy difference between initial and final halo and on the assumption that the orbital energy lost by the clump is absorbed by (the inner parts of) the halo.

Assuming spherical symmetry, let $M_i(r)$ and $M_f(r)$ denote the cumulative mass profiles of the initial and final halo. At large radii the halo is hardly altered, i.e. $M_f(r) \approx M_i(r)$, while at small radii the halo has been heated resulting in an expansion and hence $M_f(r) < M_i(r)$. A quantitative relation between the change in $M(r)$ and the mass m_s of the clump can be obtained by considering the total energy budget. By virtue of the virial theorem, the total energy of the initial equilibrium halo is half its potential energy V_i, to which the kinetic energy of the clump and the interaction energy between clump and halo must be added to obtain the total energy of the initial state (neglecting the clump self-energy):

$$E_i = \frac{m_s}{2}\left(\upsilon_i^2 + \Phi_i(r_i)\right) + \frac{1}{2}V_i, \tag{4}$$

with r_i and υ_i the initial radius and speed of the clump and $\Phi_i(r)$ the potential due to the initial halo. Expressing this in terms of the initial specific orbital energy $\varepsilon_s \equiv \frac{1}{2}\upsilon_i^2 + \Phi_i(r_i)$ of the clump and the cumulative mass profile gives

$$E_i = m_s\left[\varepsilon_s - \frac{1}{2}\Phi_i(r_i)\right] - \frac{G}{4}\int_0^\infty \frac{M_i^2(r)}{r^2}\,\mathrm{d}r, \tag{5}$$

where we have used the relation $V = -(G/2)\int_0^\infty M^2(r)\,r^{-2}\,\mathrm{d}r$. For the final state (halo in equilibrium with the clump at rest in the centre) we have

$$E_f = \frac{m_s}{2}\Phi_f(0) - \frac{G}{4}\int_0^\infty \frac{M_f^2(r)}{r^2}\,\mathrm{d}r \tag{6}$$

– this is obtained as $E = V/2$ using $M(r) = m_s + M_f(r)$ (assuming a point-mass clump) and ignoring the clump self-energy. If the clump is extended with cumulative mass profile $m_s(r)$, then $\Phi_f(0)$ in equation (6) has to be replaced by

$$\tilde{\Phi}_{f0} = -\frac{G}{m_s}\int_0^\infty \frac{m_s(r)M_f(r)}{r^2}\,\mathrm{d}r. \tag{7}$$

Equating $E_i = E_f$ and re-arranging gives

$$m_s\left(\varepsilon_s - \frac{\Phi_i(r_i) + \tilde{\Phi}_{f0}}{2}\right) = \frac{G}{4}\int_0^\infty \frac{M_i^2(r) - M_f^2(r)}{r^2}\,\mathrm{d}r > 0. \tag{8}$$

This equation relates the clump mass and its initial conditions with the change in the halo mass profile. Because this latter is a one-dimensional function, while relation (8) provides only a single constraint, it can be satisfied by many possible functional forms for the final mass profile $M_f(r)$. However, using some simple yet reasonable models for the final mass profile $M_f(r)$ we can obtain some quantitative estimates for the amount of mass excavated,

$$\Delta M(r) \equiv M_i(r) - M_f(r), \tag{9}$$

in particular its maximum and the radius at which it occurs, and their dependence on clump mass and initial specific energy ε_s.

In order to compare directly to our simulations, we chose the same initial halo density profile, given in equation (12), as used in the simulations. For the final halo we assume two different families of models; the first have mass profile

$$M_f(r) = \left(\frac{r}{x}\right)^{\gamma_i - \gamma_0} M_i(r) \quad \text{with } x^\eta = r^\eta + r_0^\eta, \tag{10}$$

where γ_i is the central density slope of the initial halo. These models have a $\rho \propto r^{-\gamma_0}$ density cusp at small radii. The second family of models also have the central density slope γ_0 and scale radius r_0 as free parameter and are given by

$$M_f(r) = M_i(r)\left(1 - \exp(-[r/r_0]^{\gamma_i - \gamma_0})\right). \tag{11}$$

The top panels of Fig. 1 show the resulting relations between clump mass m_s, obtained for the above models from equation (8), and the ratio of the maximum excavated mass over the clump mass, $\Delta M_{\max}/m_{\mathrm{s}}$, for a clump on an orbit with initial specific energy of $\varepsilon_{\mathrm{s}} = -0.12$ (left, corresponding to a circular orbit at the halo half-mass radius), or an initially parabolic orbit ($\varepsilon_{\mathrm{s}} = 0$, right) decaying in a halo with initial density (12), as used in our *N*-body simulations below. While these two types of models result in a range of values for the excavated mass, both models suggest that a clump of 1 per cent of the halo mass can excavate about 1.7 times its own mass for $\varepsilon_{\mathrm{s}} = -0.12$ and twice its own mass for $\varepsilon_{\mathrm{s}} = 0$. The models of equation (11) also indicate that a less massive clump is relatively more efficient in that it removes a larger multiple of its own mass.

The radius $r_{\max}$ at which $\Delta M(r)$ becomes maximal (and hence $\rho_{\mathrm{i}} = \rho_{\mathrm{f}}$) is shown in the middle panels of Fig. 1, again as function of clump mass m_{s}. For a clump of only 1 per cent of the halo mass, this radius can easily reach the dark matter scale radius. We also plot in the bottom panels the radius $r_{0.5}$ inside of which half the mass has been removed, i.e. $M_{\mathrm{f}}(r_{0.5}) = (1/2)M_{\mathrm{i}}(r_{0.5})$, which is readily measured from our *N*-body simulations below and provides a more direct measure of the size of any possible density core. The rankings between the models of equation (11) (solid curves in Fig. 1) with respect to $r_{\max}$ and $r_{0.5}$ are opposite to each other: the model with the smallest $r_{0.5}$ has the largest $r_{\max}$ and γ_0 and vice versa. While both $r_{0.5}$ and $r_{\max}$ clearly increase with m_{s}, as one would expect, this dependence is rather weak, approximately $r \propto m_{\mathrm{s}}^{0.6}$ for the models of equation (11) near $m_{\mathrm{s}} = 0.01M_{\mathrm{halo}}$.

Note that in obtaining these estimates we have assumed that the final halo is spherical and in perfect equilibrium. In reality, the momentum of the infalling clump is absorbed by the inner halo, which as a consequence moves slightly with respect to its outer parts. This motion is only weakly damped and it takes some time before its energy is transformed into internal heat. This implies that the estimates for $\Delta M_{\max}$ from equation (8) (as used in Fig. 1) are possibly somewhat too high, depending on the amount of energy absorbed into such oscillations. The inner asphericity resulting from the absorbed momentum also implies that the simple model spherical overestimates $\Delta M_{\max}$ (because it underestimates E_{f} given M_{f}).

3 MODELLING APPROACH

The above energy argument is only suggestive and cannot predict the final mass profiles and its dependence on the details of the satellite orbit and the initial halo equilibrium. To this end numerical (*N*-body) simulations are required. Recently, Jardel & Sellwood (2009) performed such simulations for a satellite starting on a circular orbit at the half-mass radius of a spherical dark matter halo model with a Navarro, Frenk & White (1995) density profile and isotropic velocities. They found that the orbital decay of a satellite with 1 per cent of the halo mass heats the dark matter and results in a density core of radius $\sim 0.2r_2$, where r_2 is the initial scale radius of the halo, the radius at which $\gamma(r) \equiv -\mathrm{d}\ln\rho/\mathrm{d}\ln r = 2$.

A study by Goerdt et al. (2010) also considered satellites on circular orbits, but for a variety of halo density profiles with different inner density slope γ. These authors were especially interested in the stalling of the orbital decay (Goerdt et al. 2006; Read et al. 2006), which depends sensitively on γ.

Assuming a circular orbit for the satellite may simplify some analytical arguments, but is certainly not very realistic. Similarly, the assumption of velocity isotropy for the dark matter is not justified and made only for convenience (so that initial conditions are easily prepared), though simulations by Arena & Bertin (2007) indicate that velocity anisotropy plays no significant role.

The aim of the present study is to extend the aforementioned simulations to more realistic initial conditions. In particular, we are interested in non-circular satellite orbits and cosmologically motivated velocity anisotropy for the dark matter. Our energy-based argument of Section 2 shows that the total amount of heating induced by the decaying satellite orbit only depends on the satellite orbit's energy, but not on its eccentricity. However, where the satellite dumps its energy, and consequently which halo particles gain energy and angular momentum, will depend on eccentricity. In order to differentiate these effects, we will present two sets of *N*-body simulations with satellite orbits of the same energy. The first set essentially extends the simulations of Jardel & Sellwood (2009) by considering satellite orbits of varying eccentricity, but same initial radius and energy as used by those authors. The second set of simulations considers parabolic orbits, whose initial orbital energy just vanishes. If it were not for dynamical friction, these orbits would just pass by the dark matter halo and never return. However, due to dynamical friction they become bound and decay to the halo centre if initially aimed sufficiently close. We consider isotropic velocities for the dark matter as well as velocity anisotropy of various degree and radial dependence. Furthermore, we investigate the effects from changing the satellite mass and/or its adopted size.

3.1 The halo model

For the density profile of the dark matter halo, we adopt a truncated spherical Dehnen & McLaughlin (2005) model, which gives an excellent fit to simulated CDM haloes and has density

$$\rho(r) \propto r^{-7/9}\left(r^{4/9} + s^{4/9}\right)^{-6}\operatorname{sech}(r/r_{\mathrm{t}}). \tag{12}$$

For $r_{\mathrm{t}} \to \infty$, this profile asymptotes to $\rho \propto r^{-7/9}$ and $r^{-31/9}$ at small and large radii, respectively, with a very smooth transition. We identify the scale radius with the radius at which $\gamma(r) = 2$ (in the limit $r_{\mathrm{t}} \to \infty$), which for these models is given by $r_2 = (11/13)^{9/4}s \approx 0.687s$ and set the truncation radius to $r_{\mathrm{t}} = 10r_2$, which we identify with the virial radius. We consider various velocity anisotropy profiles; in particular models for which

$$\beta \equiv 1 - \frac{\sigma_\theta^2 + \sigma_\phi^2}{2\sigma_r^2} \tag{13}$$

is constant, and models for which

$$\beta(r) = \beta_\infty \frac{r^{4/9}}{s^{4/9} + r^{4/9}}. \tag{14}$$

These latter models are isotropic in the centre and become increasingly radially anisotropic (for $\beta_\infty > 0$) at large radii, again with a very smooth transition, and are excellent descriptions of *N*-body CDM haloes (Dehnen & McLaughlin 2005).

To generate initial *N*-body conditions for the halo, we sample positions from equation (12) and velocities from self-consistent distribution functions of the form $L^{-2\beta}f(\varepsilon)$ for constant β models with $f(\varepsilon)$ obtained from an Abel inversion (Cuddeford 1991). For models with $\beta(r)$ as in equation (14), we generate initial conditions using the made-to-measure *N*-body method of Dehnen (2009).

For models with constant β, the resolution in the inner parts is enhanced by increasing the sampling probability by a factor $g(\varepsilon)^{-1}$ which is compensated by setting particle masses μ_{i} proportional to $g(\varepsilon_{\mathrm{i}})$. We used

$$g(\varepsilon) \propto \frac{1 + q\, r_{\mathrm{circ}}^{4/9}(\varepsilon)}{r_{\mathrm{circ}}^{4/9}(\varepsilon) + s^{4/9}}, \tag{15}$$

with $q = 10$ the ratio between maximum and minimum particle mass, and $r_{\mathrm{circ}}(\varepsilon)$ the radius of the circular orbit with specific energy

Table 1. Initial conditions and results for our simulations. Initial conditions are specified by the satellite size r_s and mass m_s, which default to $r_\mathrm{s} = 0.03$ and $m_\mathrm{s} = 0.01$, respectively; the pericentric radius r_peri of the initial satellite orbit; the halo initial velocity anisotropy β_i, which is either constant or $\beta(r)$ given by equation (14) with $\beta_\infty = 1$. As results we list the time t_infall for the satellite to fall to the centre of the halo (defined in Section 4.1); the radius r_max of maximum halo mass reduction ΔM_max (compared to the control simulation); the radius $r_{0.5}$ where the cumulative mass is reduced to 50 per cent compared to the control simulation; the radius $r_{M=m_\mathrm{s}}$ within which the final halo mass equals m_s and the maximum (over all radii) of ρ/σ^3 for the final halo.

r_s, m_s	r_peri	β_i	t_infall	r_max	ΔM_max	$r_{0.5}$	$r_{M=m_\mathrm{s}}$	$\max\{\frac{\rho}{\sigma^3}\}$
Simulations started at $r_\mathrm{i} = 4$ and run until $t = 1000$								
Default	0.00	−0.43	44.1	0.704	0.0157	0.330	0.315	1.36
Default	1.03	−0.43	111.4	1.351	0.0104	0.119	0.253	4.16
Default	2.44	−0.43	169.8	1.864	0.0085	0.100	0.247	4.80
Default	4.01	−0.43	198.0	2.052	0.0081	0.109	0.247	4.44
Default	0.00	0	43.5	0.646	0.0139	0.324	0.312	1.14
Default	1.03	0	99.9	0.778	0.0106	0.165	0.266	2.84
Default	2.44	0	163.1	0.783	0.0086	0.100	0.250	3.88
Default	4.01	0	193.6	0.779	0.0084	0.097	0.249	3.57
Default	0.00	0.3	43.2	0.563	0.0139	0.350	0.325	0.84
Default	1.03	0.3	87.1	0.644	0.0104	0.242	0.287	1.42
Default	2.44	0.3	145.9	0.641	0.0088	0.127	0.262	2.46
Default	4.01	0.3	178.8	0.665	0.0082	0.128	0.257	2.37
$r_\mathrm{s} = 0.01$	4.01	0	181.8	0.802	0.0084	0.048	0.247	4.67
$r_\mathrm{s} = 0.1$	4.01	0	231.1	0.464	0.0076	0.215	0.272	2.60
$m_\mathrm{s} = 0.003$	4.01	0	491.4	1.932	0.0028	0.042	0.116	13.38
$m_\mathrm{s} = 0.03$	4.01	0	90.3	1.278	0.0210	0.257	0.541	0.88
Simulations started at $r_\mathrm{i} = 10$ and run until $t = 2000$								
Default	0.0	−0.43	225	0.802	0.0243	0.530	0.384	0.86
Default	0.4	−0.43	460	0.891	0.0208	0.393	0.332	1.26
Default	0.8	−0.43	835	1.271	0.0180	0.207	0.280	2.96
Default	1.3	−0.43	1365	1.922	0.0163	0.094	0.256	4.32
Default	0.0	0	215	0.701	0.0229	0.515	0.378	0.69
Default	0.4	0	408	0.734	0.0197	0.447	0.352	0.82
Default	0.8	0	774	0.906	0.0167	0.331	0.315	1.20
Default	1.3	0	1319	1.288	0.0138	0.265	0.294	1.62
Default	0.0	0.3	202	0.710	0.0220	0.511	0.380	0.57
Default	0.4	0.3	388	0.721	0.0193	0.445	0.355	0.69
Default	0.8	0.3	700	0.750	0.0178	0.389	0.339	0.88
Default	1.3	0.3	1165	0.853	0.0160	0.358	0.329	0.84
Default	0.0	$\beta(r)$	183	0.858	0.0187	0.445	0.372	0.52
Default	0.4	$\beta(r)$	320	0.812	0.0182	0.435	0.368	0.53
Default	0.8	$\beta(r)$	593	0.807	0.0157	0.379	0.350	0.66
Default	1.3	$\beta(r)$	947	0.844	0.0159	0.372	0.348	0.65
$r_\mathrm{s} = 0.01$	0.4	$\beta(r)$	249	0.834	0.0174	0.412	0.360	0.58
$r_\mathrm{s} = 0.1$	0.4	$\beta(r)$	566	0.822	0.0177	0.415	0.360	0.65
$m_\mathrm{s} = 0.003$	0.4	$\beta(r)$	1902	0.406	0.0064	0.207	0.180	2.02
$m_\mathrm{s} = 0.03$	0.4	$\beta(r)$	95	1.149	0.0427	0.871	0.762	0.16

ε. The gravitational forces were computed using a softening kernel with density profile given in equation (16) below and r_s replaced by the softening length $\epsilon = 0.005$. Testing this method for our particular purposes we found that it allows a reduction of N by half at the same central resolution without any adverse effects.

We use a unit system where $G = M = r_2 = 1$, which implies a time unit of $15.5\,\mathrm{Myr}\,(r_2/500\,\mathrm{pc})^{3/2}(M/10^8\,\mathrm{M}_\odot)^{-1/2}$.

3.2 Orbital and other parameters of the infalling clump

Henceforth, we shall use the term ‘satellite’ for the infalling baryonic clump, which we model as a single massive extended (softened) particle. For the satellite mass m_s we considered 0.3, 1 and 3 per cent of the total halo mass (only 77 per cent of which is inside r_t associated with the virial radius), while the satellite size r_s was taken to be 0.01, 0.03 or 0.1 times the halo scale radius. This means that the satellite is effectively modelled to have spherical density profile:

$$\rho_\mathrm{s}(r) = \frac{15}{8\pi}\frac{r_\mathrm{s}^4\, m_\mathrm{s}}{(r^2 + r_\mathrm{s}^2)^{7/2}}. \tag{16}$$

We considered a large range of initial satellite orbits, but report here only on two sets of simulations. The simulations of the first set, summarized in the top half of Table 1, all start from $r = 4$, the radius containing 40 per cent of the total or 54 per cent of the mass within r_t, and have specific orbital energy $\varepsilon_\mathrm{s} = -0.12$ equal to that of the circular orbit at that radius. The only remaining free parameter of these orbits is the pericentric radius of the initial orbit – owing to dynamical friction, the actual trajectory of the satellite may have a slightly smaller first pericentric radius. These simulations thus extend those reported by Jardel & Sellwood (2009) to non-zero eccentricity and also anisotropic halo velocity distributions. The second set of simulations, summarized in the bottom half of Table 1, employs parabolic orbits, i.e. with initial orbital energy $\varepsilon_{\rm s} = 0$, started at $r = r_{\rm t}$, corresponding to the halo virial radius. Again, the only free orbital parameter is the pericentric radius of the initial orbit.

Within either set of simulations the specific energy of the initial orbit is the same. This choice was motivated by the analytic argument of Section 2, which suggested that orbital energy is the main parameter affecting the amount of 'damage' done to the halo. Thus keeping this energy fixed and varying orbital eccentricity or, equivalently, the pericentric radius, we can study the influence of this secondary orbital parameter.

3.3 Technicalities

The N-body simulations are performed using the public N-body code GYRFALCON which uses the $\mathcal{O}(N)$ force solver FALCON (Dehnen 2002) with minimum opening parameter $\theta_{\rm min} = 0.5$ and employs an adaptive time-stepping scheme.

The simulations were run for 1000 or 2000 time units for the first and second set of simulations, respectively. The energy conservation was typically 1 part in 10^4 (more accurate control simulations obtained the same results). Halo models with constant β had 1 Mio particles selected using the resolution-enhancement method of Section 3.1, while for halo models with $\beta(r)$ as in equation (14) 2 Mio equal-mass particles were used. In order to ensure a careful modelling of the satellite, it was integrated with a shorter time-step than most halo particles and the mutual forces with the halo particles were approximated with a much reduced opening angle. One simulation over 1000 time units (16 000 block-steps or 256 000 shortest time-steps) took about 190 CPU hours (single CPU, $N = 1$ Mio), including some of the analysis.

After each time-step the position and velocity of the halo centre was estimated from the position of the most bound particles.[1] Snapshots are stored at regular intervals and analysed in terms of their radial profiles using two different approaches. The first employs simple averages over radial shells, assuming the centre to coincide with the one found from the most bound particles. The second estimates for each particle the density as a kernel estimate from its 32 nearest neighbours and then computes the centre, radius and other properties from density bins. This latter method is more robust in case the configuration is non-spherical, either because of flattening or because of a spatial or velocity offset of the inner with respect to outer regions.

For all except one halo model, simulations in isolation maintained the original density profile over 2000 time units, except for the very inner parts, where artificial two-body relaxation and force softening result in a slight expansion. More quantitatively, the Lagrange radii containing $\lesssim 1 \times 10^{-3}$ of the total mass expand noticeably (see bottom panels of Fig. 2), which is more pronounced in halo models with radially biased velocity distributions. The exception is the halo model with initial $\beta(r)$ following equation (14) with $\beta_\infty = 1$. This model turned out to be unstable to the radial-orbit instability and spontaneously re-arranges into a triaxial configuration within ∼200 time units. In the course of this process the radial mass distribution is also slightly altered even without infalling satellite. In order to minimize the effects of these problems when interpreting our results, we compare each simulation with infalling satellite to a control simulation without satellite but identical initial halo. Table 1 shows a numerical summary of our results.

4 ORBITAL DECAY

In Fig. 2, we plot the time evolution of the satellite orbital radius and energy (top and middle panels) and the halo Lagrange radii (bottom panels) for both sets of satellite orbits in a dark matter halo with isotropic velocities. In all these simulations the satellite mass and size are at their default values of $m_{\rm s} = 0.01$ and $r_{\rm s} = 0.03$.

4.1 Initial orbital decay

We start our discussion by comparing the circular orbit starting at $r = 4$ (red in the left-hand panels), which is similar to that used by Jardel & Sellwood (2009), and a plunging, almost radial, orbit with vanishing orbital energy (blue in the right-hand panels of Fig. 2). While both orbits decay to the centre, their evolution is clearly different. The circular orbit decays first slowly then faster, whereby remaining near circular. The rate of decay, as indicated by the energy loss, is continuously increasing as the orbit comes closer to the centre. This is qualitatively consistent with Chandrasekhar's formula (1), since the halo density is steeply increasing inwards.

The plunging parabolic orbit (blue in the right-hand panels) on the other hand, suffers noticeable energy loss only near pericentre, undergoing a stepped rather than steady decay of orbital energy. At the first pericentric passage, the satellite loses enough orbital energy to find itself on a bound but highly eccentric orbit which returns to the inner parts of the halo within about four halo half-mass dynamical times. The energy loss at the second pericentric passage is larger, resulting in a quick orbital decay thereafter. The time-scale (note the different the time axes in the left- and right-hand panels of Fig. 2) for the decay of this orbit is only about twice as long as that of the circular orbit starting much closer (a circular orbit starting at $r_{\rm t}$ does not decay within 1000 time units). Thus, even though more energy has to be lost for this orbit, the dynamical friction at pericentre is so strong that the decay is still quite fast, even though the orbit spends about half its time well outside the halo virial radius.

During the first few periods, the pericentric radius for this plunging orbit is hardly decaying. This is expected if dynamical friction causes a near-instantaneous deceleration at pericentre, which transfers the satellite to an orbit with the same pericentric radius. The apparent decay of the pericentric radius after two periods is not because dynamical friction away from pericentre becomes significant, as the closest approach to the origin (as opposed to the halo centre) is in fact increasing, but because the centre of the halo has moved, as a consequence of the satellite interaction.

For all orbits, we identify as the orbital decay or infall time $t_{\rm infall}$ the time at which the difference $\varepsilon_{\rm s} - \Phi_{\rm h}(0)$ first obtains 2 per cent of its original value. There is a systematic trend of the infall time to decrease for higher eccentricities (smaller $r_{\rm peri}$ within each set of simulations), which is easily understood by the fact that dynamical friction is stronger for the higher density at smaller radii.

---

[1] Let ϕ denote a halo particle's specific potential energy due to all other halo particles (but not the satellite), then we first find the particle with the smallest (most negative) ϕ and its $K = 256$ spatially nearest neighbours. Then we obtain the centre position and velocity as weighted average from the $K/4$ most bound particles (with largest $|\phi|$) using the weights $|\phi_{K/4} - \phi_{\rm i}|^3$.

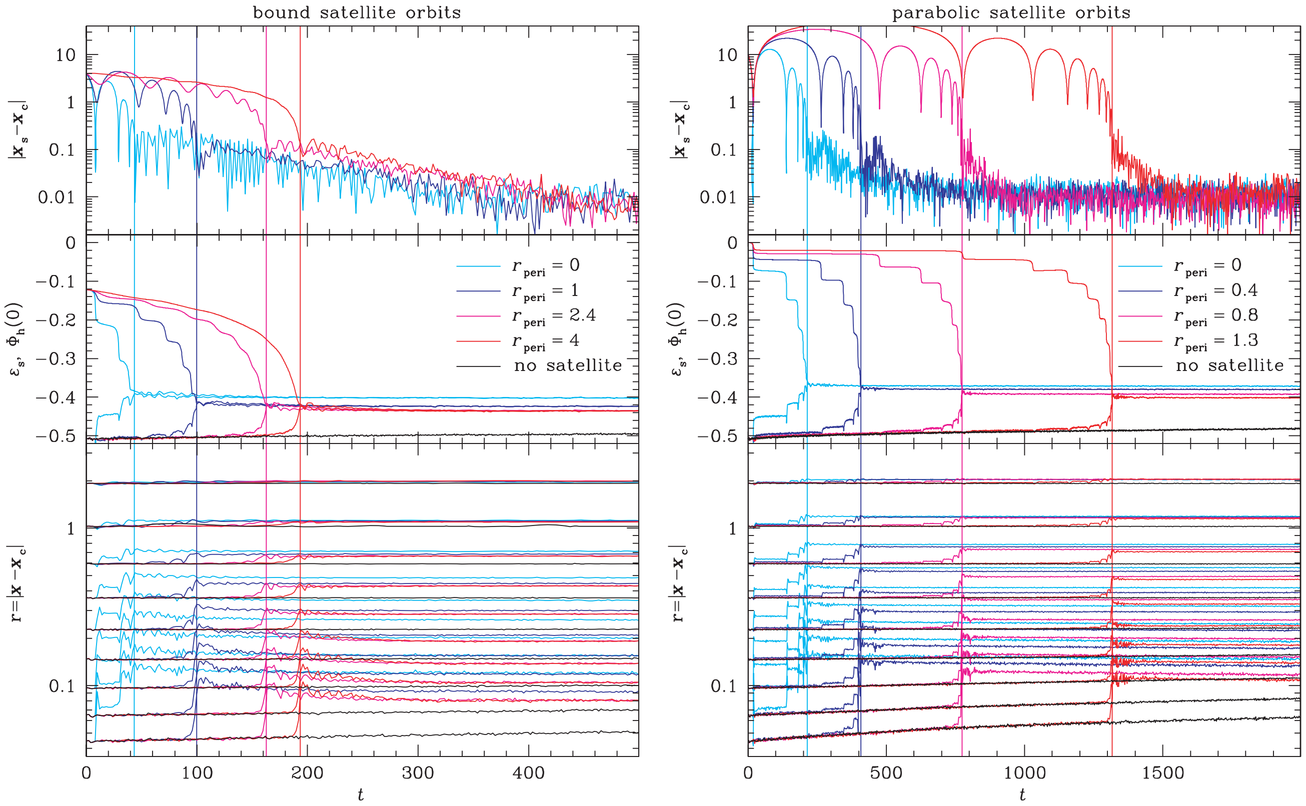

Figure 2. Time evolution of the satellite orbits and halo Lagrange radii for four bound (left) and four parabolic satellite orbits (right) decaying in a halo with isotropic velocity distribution – note the different time-scales. The top and middle panels show the evolution of the satellite distance to the halo centre and the satellite orbital energy ε_{s}, respectively. Also shown in the middle panel is the halo's central potential depth $\Phi_{\mathrm{h}}(0)$ (lower curves). The thin vertical lines indicate the time at which the difference $\varepsilon_{\mathrm{s}} - \Phi_{\mathrm{h}}(0)$ is reduced by a factor of 50. The bottom panel shows the evolution of the halo Lagrange radii (with respect to the halo centre) containing 0.08 per cent, 0.16 per cent, etc. up to 20.48 per cent of the halo mass. Within each set of orbits the initial orbital energy is the same, namely $\varepsilon_{\mathrm{s}} = 0$ for the parabolic orbits and $\varepsilon_{\mathrm{s}} = -0.12$ for the bound orbits, equivalent to that of the circular orbit at the halo half-mass radius (which is in fact the red orbit in the left-hand panels). The purely radial orbits of both sets are plotted in cyan, while the colour sequence to red corresponds to ever less eccentric orbits, reaching $e = 0$ (circular) for the family of bound orbits, corresponding to larger pericentric radii as indicated.

4.2 Late orbital decay

Interestingly, after the initial decay, when the orbital energy has almost reached its final value, the satellite and the halo centre are still orbiting each other at a distance of initially $r \sim 0.1$. In other words, the orbital decay was incomplete and has stalled. Unlike the situation investigated by previous authors, this stalling occurs at a radius which contains much less dark mass than the satellite mass m_{s} and it seems more apt to say the halo centre orbits the satellite.

This small orbit remains inert only for a short while (when $|\boldsymbol{x}_{\mathrm{s}} - \boldsymbol{x}_{\mathrm{c}}|$ remains constant or even increases at ∼0.1; see also Fig. 13), which is longer for high eccentricities of the initial orbit, while for the initially circular orbit ($r_{\mathrm{peri}} = 4$) there is hardly any such stalling. After this brief pause, the orbit decays very nearly exponentially with radial e-folding time of ∼90 time units for the bound orbits (left-hand panels of Fig. 2), which is discernable for over two e-foldings until the orbital radius reaches the noise level. In case of initially parabolic satellite orbits (right), the stalled orbits are more eccentric and their decay more erratic (but qualitatively similar) with a longer decay time (e-folding time of ∼160).

Remarkably, the secondary decay times are very similar between orbits within either set of simulation, but differ between them. This implies that the eccentricity of the initial and also the stalled orbit are not affecting the process responsible for this phenomenon. The differences in secondary decay times may be caused by differences, induced by the orbital decay, in the structure of the central halo, as discussed below.

This secondary decay is not associated with any significant orbital energy loss and has no measurable effect on the final halo density profile (except perhaps for the innermost 0.1 per cent of the halo mass), which is the main interest of our study. However, it is certainly an interesting stellar dynamical phenomenon deserving further investigation.

5 EFFECT ON THE HALO

We now discuss the changes induced by the satellite's orbital decay in the dark matter halo, concentrating mostly on the spatial distribution, while the changes to the velocity structure are mostly discussed in the next section.

5.1 Halo expansion

The middle panels of Fig. 2 also show the evolution of the central halo potential $\Phi_{\mathrm{h}}(0)$ (lower curves; not including the contribution of the satellite), which at late time coincides with the satellite's orbital energy. In all simulations, the final central potential depth of the halo is considerably shallower than initially, indicating a

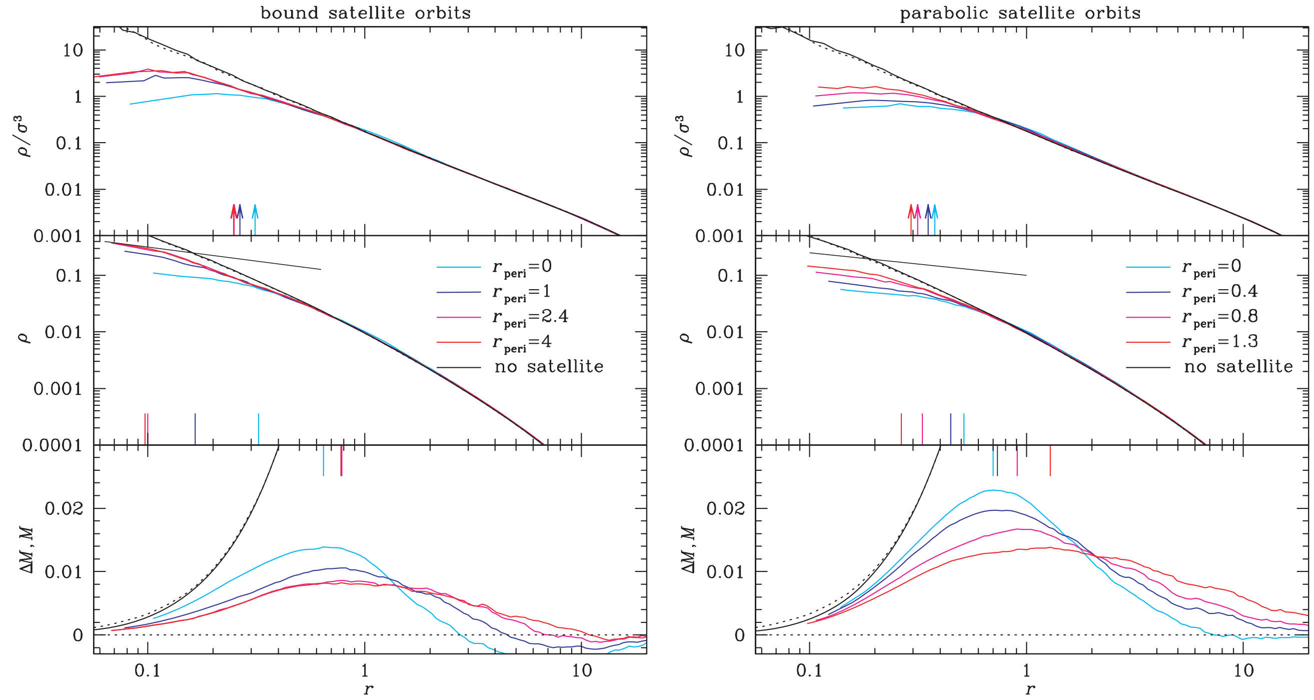

Figure 3. Radial profiles of the halo's pseudo-phase-space density ρ/σ^3 (top), density ρ (middle) and the change in cumulative halo mass ΔM (bottom) at $t =$ 1000 and 2000 for simulations of the decay of bound (left) and parabolic (right) satellite orbits, respectively. The simulations and colour coding are the same as in Fig. 2. For each model, the vertical lines in the middle and bottom panels indicate the locations of $r_{0.5}$ and $r_{\rm max}$, respectively, while the arrows in the top panels indicate the radius $r_{M=m_{\rm s}}$ within which the dark mass equals the satellite mass. The dotted curves correspond to the situation before satellite infall (t = 0), while the solid black curves represent the control simulation (no satellite). In the bottom panels, the black curves give $M(r)$, not $\Delta M(r)$. The thin black lines in the middle panels are power laws $r^{-0.5}$(left) and $r^{-0.4}$ (right).

significant reduction of the central dark matter concentration. A comparison between the various simulations also shows that this reduction is more pronounced for parabolic than for bound satellite orbits, exactly as our analytic arguments of Section 2 predicted, as well as for more eccentric orbits.

In the bottom panels of Fig. 2, we plot the time evolution of the halo Lagrange radii, while Fig. 3 shows for the same simulations the halo density ρ before and after the satellite infall, as well as the change (9) in the cumulative halo mass profile and in the pseudo-phase-space density ρ/σ^3. From the time evolution of the Lagrange radii, we see that the expansion of the inner halo occurs rather suddenly at the time when the satellite settles in the core,[2] in particular for the initially circular orbit (red in the left-hand panels of Fig. 2). For more eccentric orbits, the early pericentre passages result in some minor expansion of the halo at radii comparable to the pericentre radius, but hardly affect the innermost halo.

The mass $\Delta M(r)$ removed from inside radius r (compared to the control simulation)[3] has different radial profiles for the various simulations. Its amplitude is generally larger after the decay of a parabolic than a bound orbit, which is due to the larger orbital energy of the former leading to stronger heating of the dark matter particles. In fact, the maximum mass excavated $\Delta M_{\rm max}$ is about twice the satellite mass if the latter is decaying on a plunging parabolic orbit, consistent with our models of Section 2, while for a circular orbit decaying from $r = 4$, corresponding to the situation studied by Jardel & Sellwood (2009), $\Delta M_{\rm max} < m_{\rm s}$. This difference between $\Delta M_{\rm max}$ obtained for orbits with $\varepsilon_{\rm s} = 0$ (parabolic) and $\varepsilon_{\rm s} = -0.12$ (bound) is even more pronounced than for the analytical models of Fig. 1.

Within each set of orbits $\Delta M(r)$ is most peaked for the purely radial orbit, while it widens for lower eccentricities. This is presumably because a satellite on a highly eccentric loses its energy to a narrow range of dark matter particles close to its pericentre, while less eccentric orbits lead to a distribution over a wider range.

5.1.1 Central density reduction

The density profiles in the middle panels of Fig. 3 confirm earlier results that the infall of a baryonic clump can considerably weaken the central dark matter cusp. The final halo mass profiles (not shown) are noticeably perturbed interior to the radius $r_{\rm max}$ (indicated by the vertical lines in the bottom panels of Fig. 3), at which by definition the final halo density equals that of the control simulation without satellite. In order to quantify further the properties of the inner halo density profiles, we also calculate the radius $r_{0.5}$ (indicated by the vertical lines in the middle panels of Fig. 3) interior to which the dark mass is reduced to 50 per cent compared to the control simulation. In general, $r_{0.5}$ is smaller than $r_{\rm max}$ and marks the radius at which significant changes to the halo density profile are evident.

There is a clear trend for more eccentric orbits to more strongly reduce the central density and hence result in a larger radial range over which the density has been significantly reduced: $r_{0.5}$ is larger for smaller $r_{\rm peri}$. The opposite is true for the radius $r_{\rm max}$. This

---

[2] The initial slow rise of the innermost Lagrange radii is entirely due to artificial two-body relaxation and not present in simulations with 10 times the number of halo particles, see also the last paragraph of Section 3.3.

[3] For the simulations, $\Delta M(r)$ is always measured this way, rather than against the initial model (as in equation 9), in order to account for halo evolution in absence of any satellite.

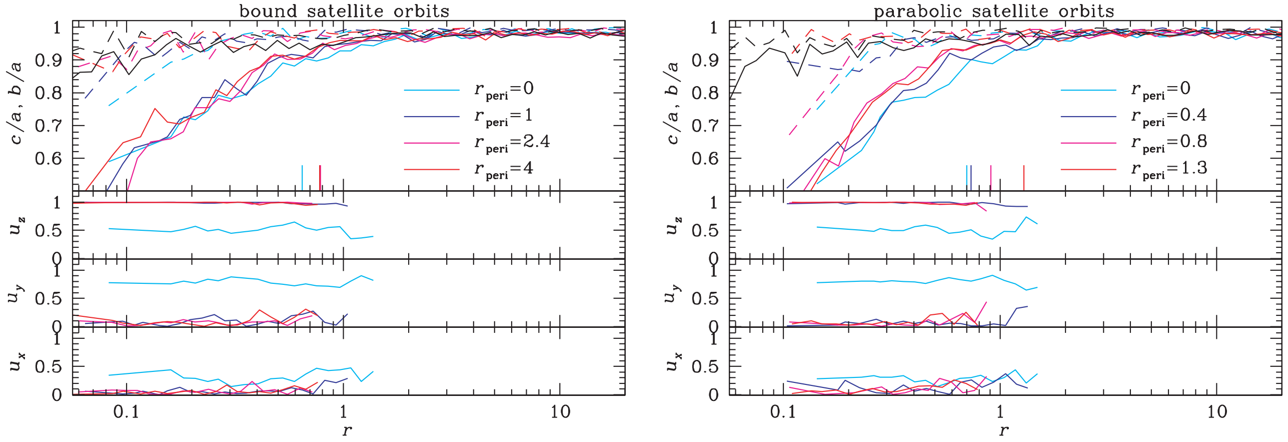

Figure 4. Radial profiles of the intermediate-to-major (*b*/*a*, dashed) and minor-to-major (*c*/*a*, solid) axial ratios, as well as the direction of the minor axis, provided as the *x*, *y* and *z* components of the unit vector along the minor axis (plotted where $c/a < 0.95$) for the final halo in the same simulations as in Figs 2 and 3. The vertical lines in the top panel indicate for each model the location of $r_{\rm max}$.

contrasting behaviour of $r_{0.5}$ and $r_{\rm max}$ can be understood in terms of the different shapes of the excavated mass distribution $\Delta M(r)$, which becomes broader with increasing $r_{\rm peri}$, presumably because the energy input is spread over a larger radial range.

Such an anticorrelation between $r_{0.5}$ and $r_{\rm max}$ for simulations with the same initial satellite orbital energy $\varepsilon_{\rm s}$ was also present in the analytic models in Fig. 1. For those analytic models the effect was generated by assuming different central density slopes $\gamma_0 = -{\rm d}\ln\rho/{\rm d}\ln r|_{r=0}$. However, the central density slope of the final *N*-body models (middle panel in Fig. 3) is remarkably similar at around $\gamma_0 = 0.4$–0.5 at radii $r \lesssim r_{0.5}$. We should stress, however, that the inner regions of these halo models are gravitationally dominated by the sunken satellite, and hence cannot be sensibly compared to the dark matter haloes of galaxies.

5.1.2 Central phase-space density reduction

We also show in Fig. 3 the radii $r_{M=m_{\rm s}}$ at which the enclosed dark mass equals that of the satellite (arrows in the top panels). Evidently, these radii do not differ much from $r_{0.5}$, implying that the innermost final dark matter profiles are not self-gravitating: their gravity is dominated by the accreted satellite. Since the satellite size $r_{\rm s} = 0.03$ is about 10 times smaller than the radius inside of which it dominates the dynamics, it is effectively acting like a central point mass. A tracer population orbiting a point mass has a cusp $\rho \propto r^{-3/2}$ if its phase-space density is constant. However, the simulations have much shallower central cusps, suggesting that the actual dark matter phase-space density has a central depression, decreasing towards the highest binding energies.

This is also borne out by the plots of the pseudo-phase-space density ρ/σ^3 in the top panels of Fig. 3: while initially and in the control simulations (dotted and solid black curves) these follow a pure power law (this is how these models are actually constructed; see Dehnen & McLaughlin 2005), the final profiles show a strong central depression, suggesting a considerable reduction of dark matter phase-space density. The corresponding reduction in spatial density is much weaker, because the available phase space is increased above that from the self-gravitating cusp by the deeper central potential due to the accreted satellite.

The central velocity dispersion initially decreases towards $r = 0$ as $\sigma^2 \propto r^{\min(\gamma,2-\gamma)}$ for a self-gravitating $\rho \propto r^{-\gamma}$ cusp. In all simulations, the final halo has $\sigma(r)$ increasing towards smaller radii (not shown, but evident from the strong central depression in ρ/σ^3 compared to that in ρ), inside the radius $r_{M=m_{\rm s}}$, as is required for any equilibrium system dominated by a central mass concentration.

5.2 Halo shape

In all our simulations, the dark matter halo is initially spherical. The top panels of Fig. 4 show the run of the final halo's principal axis ratios for the same simulations as in Figs 2 and 3. At $r \lesssim 1.5 > r_{\rm max}$ the final dark matter distribution is near-oblate in all cases, becoming flatter towards the centre at reaching $c/a \sim 0.5$ at the smallest measurable radius. The bottom panels of the same figure show the direction cosines of the minor axis. Note that the satellite initially orbits in the *x*–*y* plane, starting at $y = 0$ and $x = r_{\rm i}$. For all but the purely radial orbits the halo minor axis is perpendicular to the initial orbital plane of the satellite. This is easily understood to originate from the transfer of orbital angular momentum from the satellite to inner halo particles during pericentric passages, which presumably also generates the oblate inner halo shape.

For the purely radial satellite orbits (cyan), which start off with zero orbital angular momentum, the final halo minor axis does not align with the satellite orbit, but appears to point in some random direction (though it is self-aligned). This behaviour is counter-intuitive as the initial models for these simulations are completely symmetric with respect to the infall axis. However, such a break of symmetry is the natural behaviour of radial orbits in the gravitational potentials of a density cusp. This is best explained by considering the limit of vanishing pericentre radius for the change in azimuth $\Delta\phi$ occurring over one radial period from apo-centre to apo-centre. For a harmonic potential, corresponding to $\gamma = 0$, the radial orbit just passes straight through ($\Delta\phi = \pi$), while in the potential generated by a point mass, corresponding to $\gamma = 3$, the radial orbit is reflected ($\Delta\phi = 2\pi$). For mass distributions with intermediate values of γ, such as dark matter haloes, $\Delta\phi$ is between these two extremes, and the symmetry of the initial orbit is broken.[4]

---

[4] Strictly speaking, the radial orbit with $L = 0$ is never deflected ($\Delta\phi = \pi$) as no transverse forces act on it. However, in the limit $L \to 0$ one gets $\Delta\phi > \pi$ (except for the harmonic potential), i.e. $\Delta\phi$ is discontinuous at $L = 0$ or, equivalently, $r_{\rm peri} = 0$. In our simulations, the halo potential is modelled from the softened particle potentials and deviates from the power law form at $r \lesssim \epsilon = 0.005$, where it becomes harmonic and the discontinuity

This deflection of the satellite orbit is compensated by an equal and opposite momentum to the inner halo, such that the subsequent relative orbit of the two is no longer radial. The further evolution follows the same pattern as for the non-radial orbits: the halo flattens perpendicular to the angular momentum axis of this orbit. Note that for both radial orbit simulations shown in Fig. 4 the minor axis is near-perpendicular to the original infall direction (x-axis). This is explained by the fact that $\Delta\phi$ for a shallow cusp is only slightly larger than the value π for the harmonic potential, implying that the orbit is only weakly deflected from its original infall trajectory, which is indeed what we see in our simulations.

There is also some hint of triaxiality at small radii, in particular for the radial bound orbit. This is somewhat surprising as it mostly occurs within the region where the satellite dominates the enclosed mass and hence the potential is near-spherical. We suspect that this very central triaxiality is generated during the secondary orbital decay if the small decaying orbit is eccentric.

6 EFFECT OF HALO VELOCITY ANISOTROPY

So far, we have discussed the results from eight simulations, which differed only in the satellite orbit, but had the same initial halo model with velocity isotropy. We are now investigating initially anisotropic dark matter velocity distributions. Since parabolic orbits are more realistic for infalling clumps, we restrict our discussion to the four satellite orbits with initially vanishing orbital energy $\varepsilon_\mathrm{s} = 0$ and various eccentricities. Most of our general conclusion are, however, at least qualitatively also valid for bound orbits.

In addition to the halo model with velocity isotropy, used in Sections 4 and 5, we consider three initially anisotropic models. Two of these have constant anisotropy parameter of $\beta = 0.3$ and -0.43, respectively, which corresponds to the same level of anisotropy in the sense of $|\ln \sigma_r/\sigma_\mathrm{t}|$ (with the tangential velocity dispersion $\sigma_\mathrm{t}^2 \equiv [\sigma_\phi^2 + \sigma_\theta^2]/2$). The third anisotropic halo model is motivated by simulations of galaxy halo formation, which generally predict that the velocity distribution of the dark matter within haloes is outwardly increasing radially anisotropic (Hansen & Moore 2006). We use the anisotropy profile of equation (14) with $\beta_\infty = 1$. This halo model is quite different from the others, as it undergoes a radial orbit instability, and we discuss it in some more detail in Section 7.

6.1 Halo phase-space structure and vulnerability

Before we discuss the simulations, let us consider an important difference between these four models. Haloes with more radially biased velocities have more mass on eccentric orbits, which spend most of their time near apo-centre, but contribute significantly to the density near their respective pericentres, in particular if the density increases more slowly than r^{-2} (because of geometrical effects) as it does in the inner regions of dark matter haloes. Consequently, much of the dark matter in the innermost region of a halo with radial velocity anisotropy is on orbits which spend most of their time outside the innermost halo and have lower binding energies than the local circular orbits. Thus the more radially biased the velocities, the less mass is at high binding energies, as demonstrated in Fig. 5, which shows the differential energy distributions dM/dE for our four halo models (computed from N-body data; for a cleaner plot of the same effect but for different models; see fig. 4.5 of Binney & Tremaine 2008).

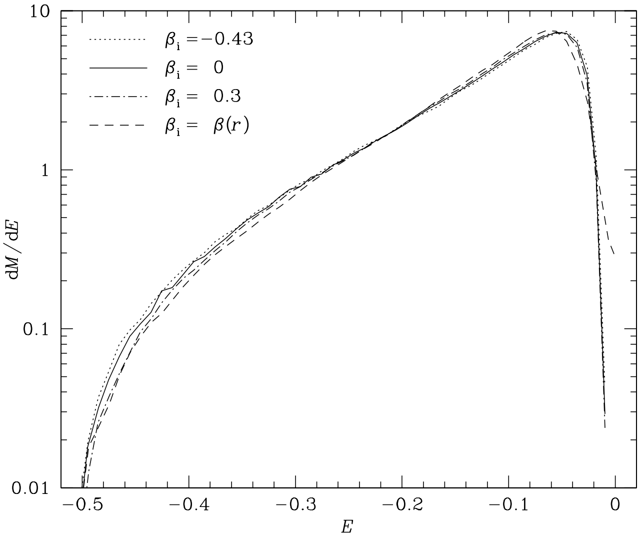

Figure 5. Differential energy distributions for the four different halo models considered, which only differ in their velocity anisotropy profiles.

The relative lack of highly bound orbits in haloes with radial velocity anisotropy has immediate consequences for the responsiveness and hence vulnerability of the central regions to perturbations, such as an infalling massive satellite (see also Binney & Tremaine 2008, p. 299). Highly bound orbits are confined to the central regions, which makes them relatively inert to external perturbations, in particular if their orbital period is short compared to the timescale of the perturbation (adiabatic invariance). The eccentric orbits in haloes with radial velocity anisotropy, on the other hand, have longer periods and hence are not adiabatically protected in the same way. Moreover, the infalling satellite can relatively easily perturb dark matter particles near the apo-centres of such orbits, increasing their angular momenta and hence pericentric radius, and thereby reducing the central density of the halo.

These arguments also suggest that the difference in vulnerability between haloes with isotropic and radially anisotropic velocities is more pronounced for perturbation by a satellite passing at larger pericentric radius, which affects eccentric orbits contributing to the centre, but hardly the innermost orbits. A satellite falling in on a purely radial orbit, on the other hand, will affect dark matter orbits at all radii, regardless of halo anisotropy.

6.2 Change in velocity anisotropy

In Fig. 6, we plot the radial β profiles of the final halo in simulations of the decay of the four different parabolic satellite orbits (colour coded as in Figs 2–4) in each of the three different halo models with constant initial β.

In case of initial velocity isotropy the final velocity distribution is isotropic too, while in all of the initially anisotropic cases, the halo velocity distribution evolves towards isotropy in the inner regions. This evolution is partly driven by (artificial) two-body relaxation, as evident from the control simulations (green in Fig. 6), which results in velocity isotropy at $r \lesssim 0.1$. However, for the simulations with decaying satellite orbit, this isotropization occurs to larger radii, which is essentially independent of the orbital eccentricity of the decaying orbit, and is only a function of the initial halo anisotropy.

---

at $r_\mathrm{peri} = 0$ is removed such that $\Delta\phi \approx \pi$ for $r_\mathrm{peri} \lesssim \epsilon$. However, even the simulations with initially purely radial satellite orbits have actual $r_\mathrm{peri} > \epsilon$ at first passage (see Fig. 2), such that the simulated satellite orbit is actually deflected.

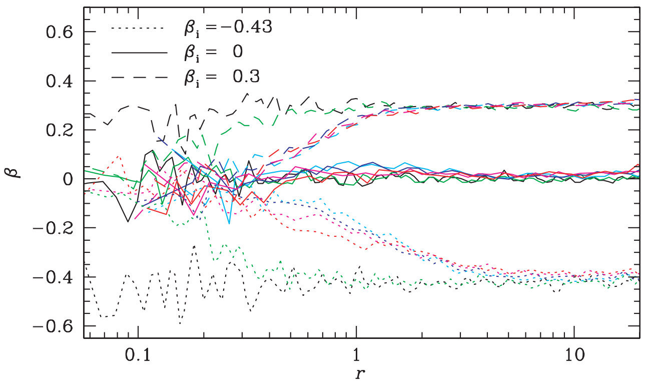

Figure 6. Radial profiles of the final (at $t = 2000$) halo velocity anisotropy parameter β for 4 × 3 simulations: four parabolic satellite orbits (as shown in the right-hand panels of Figs 2–4 with the same colour coding) decaying in three halo models with different constant initial anisotropy (line style as indicated). The black and green curves are the radial anisotropy profiles (obtained in the same way from N-body data) of the initial conditions and the control simulations, respectively. The satellite mass and size are $m_s = 0.01$ and $r_s = 0.03$ (as for all simulations presented so far).

This radius is larger by about a factor of 3 for the models with initially constant tangential velocity anisotropy than for the models with initially constant radial velocity anisotropy. This is somewhat surprising in view of the discussion in the previous subsection. One speculation is that a system with tangential velocity anisotropy is not well mixed in the sense of Tremaine, Henon & Lynden-Bell (1986) and Dehnen (2005), such that violent relaxation, induced by the perturbation, promotes evolution towards isotropy, while perhaps the opposite is true for radial velocity anisotropy.

It is also interesting to note that the evolution of the anisotropy profile is complete by the time of the first qualitative change in the orbit (i.e. essentially at $t = t_{\rm infall}$). Thereafter, the final secondary decay of the satellite orbit takes place without further modification of the halo velocity distribution.

6.3 Effect on orbital decay and final halo

Instead of showing detailed figures, similar to Figs 2–4, of the time evolution and radial profiles of density, axis ratios, etc. for the final halo of all the 4 × 4 simulations, we summarize the effects of different initial halo anisotropy in Fig. 7, which shows, for each simulation, the infall time $t_{\rm infall}$ as well as several properties of the final halo (at $t = 2000$). Apart from $\Delta M_{\rm max}/m_s$, $r_{\rm max}$ and $r_{0.5}$, already used in previous sections, we also plot the maximum value for the pseudo-phase-space density ρ/σ^3 and the radius inside of which the minor-to-major axial ratio $c/a < 0.8$.

There is a systematic trend of shorter infall times for initially more radial dark matter velocity anisotropy, exactly as expected from the arguments of Section 6.1: the inner parts of haloes with radially biased velocities are more responsive to and vulnerable by the infalling satellite. This is also the reason for the behaviour of $r_{0.5}$ and $\max\{\rho/\sigma^3\}$, which demonstrate that haloes with initially more radial velocity anisotropy suffer the strongest reduction in their central density and phase-space density. As argued in Section 6.1, the effects of initial halo velocity anisotropy are most pronounced for satellite orbits with large $r_{\rm peri}$ and least for a purely radial satellite orbit.

Again, the radius $r_{\rm max}$ at which $\Delta M(r)$ peaks anticorrelates with the radius $r_{0.5}$, indicating that the distribution $\Delta M(r)$ becomes more peaked (not shown) for more radially biased velocities and that this peak occurs at smaller radii. Both of these are natural consequences of the difference in orbital structure as outlined above.

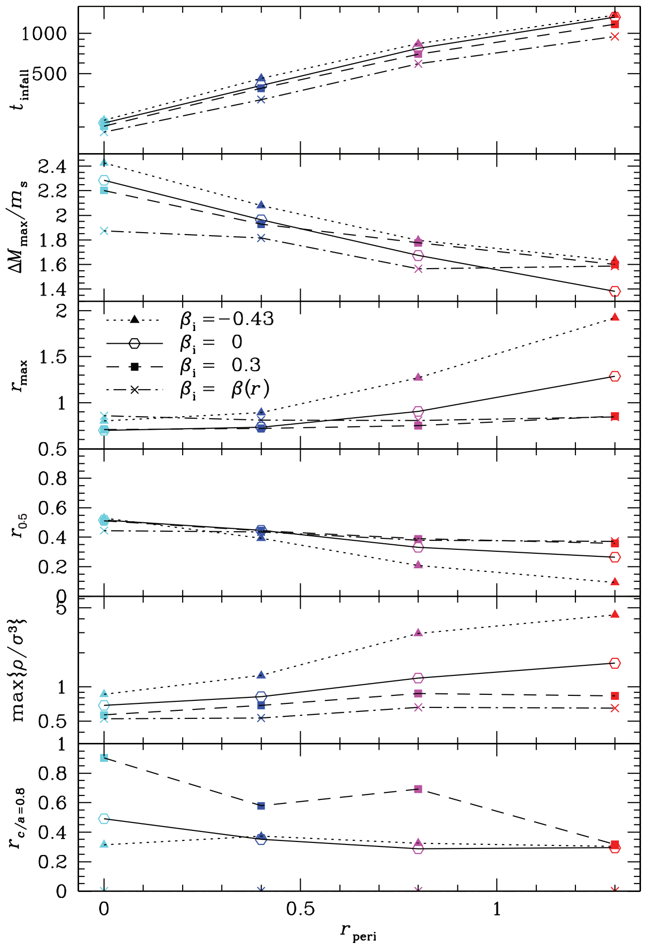

Figure 7. Dependence of orbital decay time $t_{\rm infall}$ and several properties of the final halo (the bottom panel plots the radius inside of which the minor-to-major axial ratio $c/a < 0.8$) on initial halo velocity anisotropy (line style as in Fig. 6) and initial pericentre for parabolic orbits with satellite of mass $m_s = 0.01$ and size $r_s = 0.03$. Symbol colours match those in Figs 2–4.

There is also a systematic effect on the halo shape. For each model with initially constant β, the bottom panel of Fig. 7 plots the radius inside of which the minor-to-major axial ratio $c/a < 0.8$. The halo with tangential velocity anisotropy becomes flattened in a region comparable to that of the halo with isotropic velocities. For the halo with $\beta = 0.3$, the flattening is more pronounced, reaching out to about twice as far, and the shape is near-oblate (not shown) with the same characteristic as for the halo with initial velocity isotropy, discussed in Section 5.2. This is again expected, as the satellite's orbital angular momentum absorbed by the halo is relatively more important for dark matter on low-angular-momentum orbits, as for radial velocity anisotropy.

7 HALO WITH COSMOLOGICALLY MOTIVATED VELOCITY ANISOTROPY

The situation with an outwardly increasing radial velocity anisotropy as in equation (14) is typical for dark matter haloes emerging from simulations of large-scale structure formation (Hansen & Moore 2006). As already mentioned in Section 3.3, our spherical halo model with such an anisotropy profile undergoes a radial-orbit instability and quickly settles into a prolate configuration. While this instability somewhat complicates the interpretation of any results, the corresponding simulations are presumably most realistic what concerns the halo structure.

7.1 Orbital decay

For the four simulations of initially parabolic satellite orbits in this halo model, we plot in Fig. 8 the orbital decay and time evolution of the halo Lagrange radii, similar to the right-hand panels of Fig. 2. First note that the control simulation (black) undergoes an initial expansion within the first ∼200 time units. This expansion is largely driven by the violent relaxation during the re-arrangement to a prolate configuration (due to the radial-orbit instability), while the expansion seen in the other control simulations (see Fig. 2) was solely driven by (artificial) two-body relaxation.

The orbital decay is faster than for any other halo model considered (see top panel of Fig. 7), because of the more efficient transfer of satellite orbital energy and angular momentum to the halo particles (as outlined in Section 6.1) during the very first pericentric passages, when the halo density is not yet diminished by the instability-driven expansion. The associated heating of the innermost halo results in a slightly faster expansion in the simulations with satellite than in the control simulation even at $r < r_{\rm peri}$.

The same is true to a lesser degree for the halo with $\beta = 0.3$ (not shown), while for the halo with isotropic velocities (Fig. 2), the Lagrange radii at $r < r_{\rm peri}$ were hardly affected by the early pericentric passages. This different response of the innermost halo to the satellite's first pericentric passage can be attributed to the predominance of eccentric dark matter orbits in the innermost halo, which are perturbed by the passing satellite at their respective apocentres, as outlined in Section 6.1.

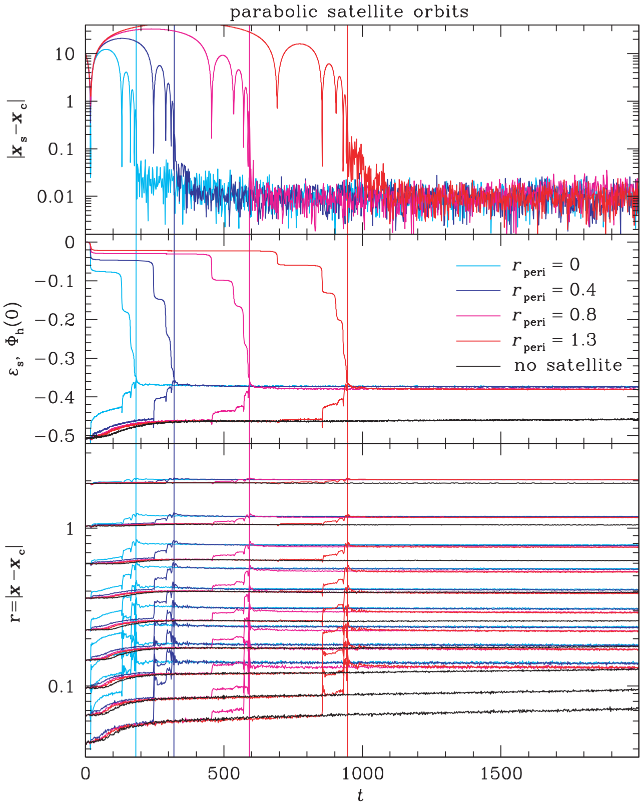

Figure 8. Like the right-hand panels of Fig. 2, but for an initial halo with cosmologically motivated velocity anisotropy profile.

7.2 Effect on halo structure

Fig. 9 shows the radial profiles of ρ/σ^3, ρ, ΔM, β, c/a, b/a and the direction cosines of the minor and major axes (similar to the right-hand panels of Figs 3 and 4) for the four simulations with decaying satellite orbits (coloured), the initial model (dotted) and

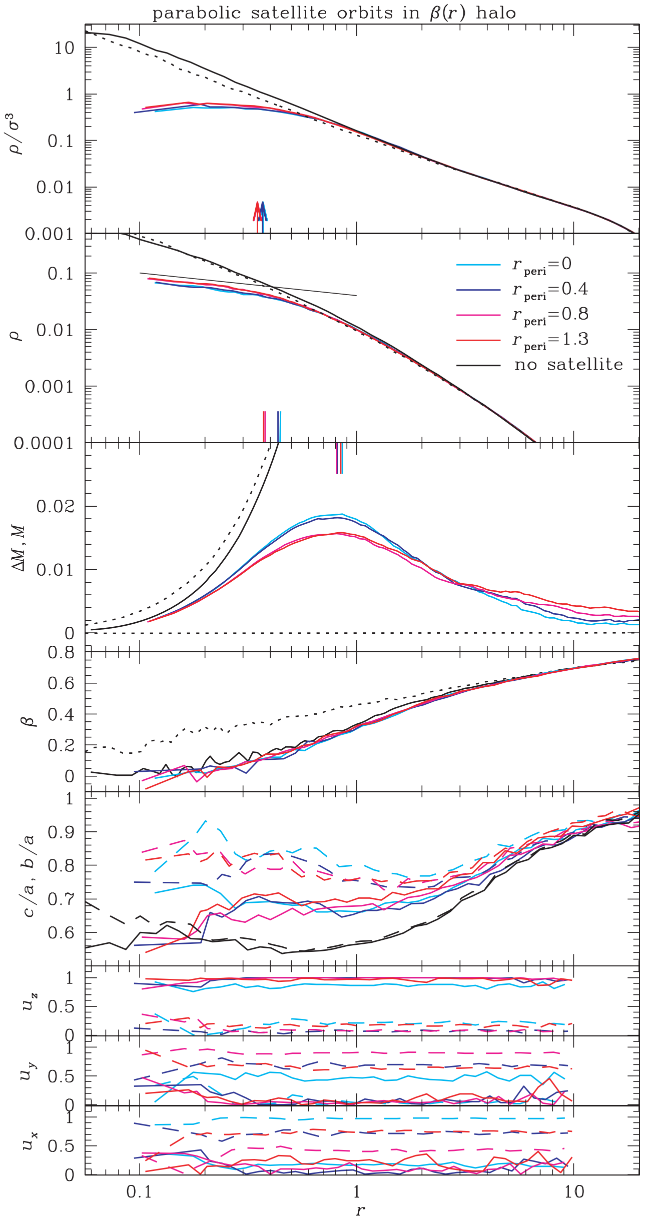

Figure 9. Final halo radial profiles after the infall of a satellite on an initially parabolic orbit into a halo with initially radially increasing velocity anisotropy $\beta(r)$ as in equation (14) with $\beta_\infty = 1$. The plots are equivalent to Figs 3 and 4 (the thin line in the density plot is $r^{-0.4}$), except that in the bottom three panels we plot not only the minor axis direction cosines (solid), but also the major axis direction cosines (dashed). For this halo model the control simulation (black) also undergoes some evolution driven by a radial-orbit instability, most evident from the changes in anisotropy and shape, see text for details.

control simulation (black). All these radial profiles after satellite orbit decay are quite similar, the strongest difference is 15 per cent between the amplitudes of $\Delta M(r)$. This similarity is also expected from our discussion in Section 6.1: the halo is so responsive that the exact satellite orbit does not matter too much.

The pseudo-phase-space density, ρ/σ^3 (top panel), of the control simulation is even larger than initially, although the density is reduced at $r \lesssim 0.15$. The reason for this counter-intuitive behaviour is that the isotropization (evident from the runs of β) has reduced the velocity dispersion σ in the inner parts. However, after the orbital decay of the satellite, ρ/σ^3 is substantially reduced and necessarily also the true phase-space density. The maximum pseudo-phase-space density is a factor of 2–3 smaller than for simulations with initial velocity isotropy, and the density a factor of ∼2. This represents the strongest central halo reduction in all models (for the default values of satellite mass and size), which makes sense in view of the vulnerability due to the radial velocity anisotropy.

The mass ΔM excavated compared to the control simulation is slightly less for the purely radial orbit (but slightly more for the orbit with $r_{\rm peri} = 1.3$) than in case of an isotropic halo (Fig. 3). However, such a comparison is not quite adequate in view of the different behaviour of the respective halo models in isolation, and the picture that stronger radial velocity anisotropy results in larger an effect on the halo remains valid.

In all simulations is the final halo more isotropic than initially at $r \lesssim 3$, but still retains significant radial anisotropy. In fact, the β profiles are identical to that of the control simulation, presumably because this profile corresponds to a well-mixed state, attained after the initial violent relaxation phase, and hardly affected by any further relaxation due to satellite interaction. Such radially anisotropic velocity distributions are likely the inevitable property of triaxial and prolate equilibria, because of the predominance of low-angular-momentum orbits, such as box orbits (Dehnen 2009).

7.3 Effect on halo shape

Obviously, the final halo shapes are completely different from those obtained in simulations with any other initial halo model. As a result of the radial-orbit instability, the control simulation obtains a strongly flattened purely prolate shape with axial ratio <0.6 at $r \lesssim 2$ (and some random orientation). This is in remarkable agreement with the fact that dark matter haloes in gravity-only simulations of large-scale structure formation tend to have near-prolate shapes (Warren et al. 1992). After the satellite infall, however, the halo shape becomes less flattened and triaxial in the inner parts. The changes in halo shape compared to the control simulation extend to about $r \sim 5$, much farther than the changes in halo density or velocity anisotropy.

As the direction cosines indicate, the orientation of the principle axes of the triaxial shape is constant with radius, as one expects for an equilibrium system. The minor axis is always perpendicular to the original satellite orbit, while the major axis is somewhere in the initial orbital plane (except for the purely radial orbit for which such a plane cannot be defined).

8 VARYING SATELLITE MASS AND SIZE

All simulations presented so far have the same satellite mass $m_{\rm s} = 0.01$ and size $r_{\rm s} = 0.03$. We now investigate effects of larger and smaller values for these parameters.

8.1 Varying satellite mass

Fig. 10 shows the effect of varying $m_{\rm s}$ by a factor of of 3 up and down for a satellite initially on a circular orbit in a halo with isotropic velocities (red) and for a satellite on a parabolic with $r_{\rm peri} = 0.4$ in a halo with cosmologically motivated $\beta(r)$. As expected, more massive satellites reach the centre more rapidly, and cause more damage to the inner halo. In agreement with Fig. 1, $r_{\rm max}$, $r_{0.5}$ and $\Delta M_{\rm max}$ are largest for the most massive satellite, and decrease systematically as the satellite mass is decreased. As the figure shows, the scaling of $r_{\rm max}$ and $r_{0.5}$ with satellite mass is close to scaling $r \propto m_{\rm s}^{0.6}$ (solid lines) also found for our analytic models in Fig. 1.

The most interesting result from this study of varying satellite mass is that low-mass satellites are more efficient at displacing mass than high-mass satellites: in agreement with the analytic models the *relative* excavated mass $\Delta M_{\rm max}/m_{\rm s}$ increases towards smaller satellite masses.

According to Chandrasekhar's dynamical friction formula (1), the drag on the satellite is proportional to its mass $m_{\rm s}$ and would therefore naively expect the infall time to scale inversely with satellite mass: $t_{\rm infall} \propto m_{\rm s}^{-1}$. This is in fact the scaling indicated by the solid lines in the top panel of Fig. 10. However, the actual infall time measured for our simulations differ from this expectation. For the simple situation of an initially circular satellite orbit in a stable halo with isotropic velocities (red triangles), the infall time-scales more like $t_{\rm infall} \propto m_{\rm s}^{-0.9}$. This difference is most likely caused by the re-adjustment of the halo during the satellite infall, an effect we ignored when deducing $t_{\rm infall} \propto m_{\rm s}^{-1}$, which therefore only applies in the limit $m_{\rm s} \to 0$. The fact that this limit is not applicable even for $m_{\rm s}/M_{\rm halo} = 0.01$ may seem surprising, but is not in view of the fact that only a small fraction of the total halo mass accounts for most of its binding energy, which in turn enables such a feeble satellite to inflict significant damage to the halo.

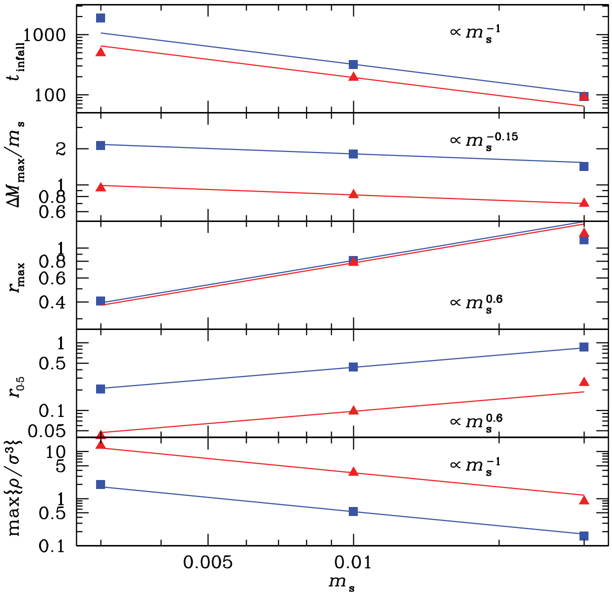

Figure 10. The variation with satellite mass of $t_{\rm infall}$, $\Delta M_{\rm max}$, $r_{\rm max}$, $r_{0.5}$ and the maximum (over all radii) of ρ/σ^3 after the decay of a circular satellite orbit starting at $r_{\rm i} = 4$ in a halo with isotropic velocities (red) or after the decay of a parabolic satellite orbit with $r_{\rm peri} = 0.4$ starting at $r_{\rm i} = 10$ in a halo with outwardly increasing radial velocity anisotropy (blue). The lines are power laws with exponent as indicated.

The orbital decay into the halo model with radially increasing $\beta(r)$ (blue squares) is complicated by the fact that the halo simultaneously undergoes a radial-orbit instability. The slight central density reduction driven by this instability increases the infall time compared to the original halo within the first ∼200 time units. In our simulations, this sets up a race between satellite infall and instability-driven halo evolution. A more massive satellite sinks more quickly than this evolution and t_{infall} of the original halo applies, while for a low-mass satellite the longer infall time after the instability-driven halo evolution applies. Clearly, this race scenario is an artefact or our simulation set-up, and we expect, based on the arguments given above, that in general t_{infall} scales slightly shallower than m_{s}^{-1}.

8.2 Varying satellite size

In Fig. 11 we vary the size r_{s} of the satellite by a factor of 3 up and down, while holding its mass fixed for a circular satellite orbit in an isotropic halo (red triangles) and a parabolic satellite orbit with $r_{\mathrm{peri}} = 0.4$ in a halo with cosmologically motivated $\beta(r)$. There is a systematic trend that more compact satellites lose energy more quickly and hence exhibit more rapid orbital decay. This is reasonable as more compact satellites are more efficient at scattering background particles and thus lose energy to the halo more rapidly.

The panels of Fig. 11 show that the cumulative effect of the satellite on the halo is almost independent of its size – the values of $\Delta M_{\mathrm{max}}/m_{\mathrm{s}}$, r_{max} and max $\{\rho/\sigma^3\}$ are virtually unchanged as the size of the satellite is changed by an order of magnitude, in particular for the parabolic orbit in the $\beta(r)$ halo. This is not very surprising in view of the analytical models of Section 2: the orbital energy of the satellite is essentially independent of r_{s} (as long as $r_{\mathrm{s}} \ll r_2$).

However, for the circular satellite orbit decaying in a $\beta = 0$ halo, there is a systematic trend of larger $r_{0.5}$ with larger r_{s} and the halo profile is more significantly flattened by a more extended satellite. This is also seen in the evolution of the Lagrange radii and is reasonable since the more extended the satellite, the less energy it loses at large radii and therefore has more energy to impart to the innermost halo. More extended satellites on near-circular orbits carry more energy to the inner regions and hence perturb the halo profile to a greater degree (for highly eccentric orbits this picture does not apply, as they affect the innermost halo already at their first pericentric passage).

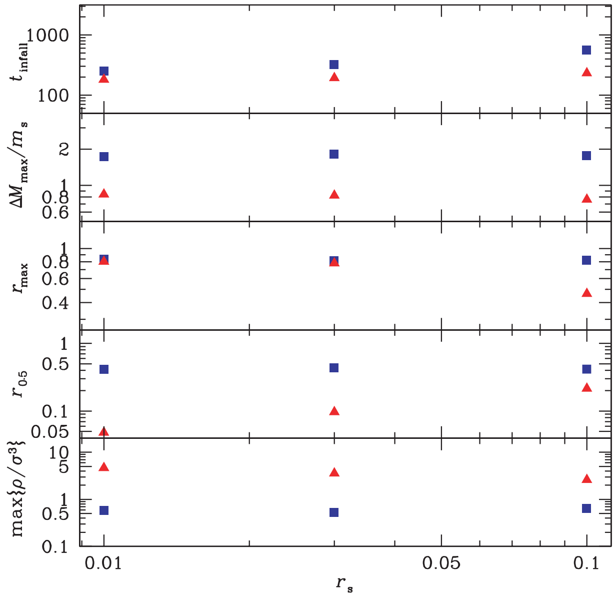

Figure 11. Like Fig. 10, except that satellite size r_{s} is varied and $m_{\mathrm{s}} = 0.01$ kept constant.

The evolution produced by satellites on bound orbits in isotropic haloes is qualitatively the same as that for parabolic orbits, although the magnitude of the effects is reduced. In particular, the infall time differs by only 30 per cent between the largest and smallest satellites, compared to the factor of 3 for the parabolic satellite orbit in the halo with increasing $\beta(r)$. This again may be caused by the increased vulnerability and responsiveness of haloes with radial velocity anisotropy, as discussed in Section 6.1.

9 THE EFFECT OF SATELLITE REMOVAL

In our modelling so far we have ignored the additional halo expansion following the possible loss of baryons in a feedback-driven galactic wind. At the final time in the models, the gravitational potential inside $\sim 0.1 r_2$ is dominated by the satellite. Therefore the central potential is still quite deep, even though for most of our models the satellite mass is somewhat smaller than the removed dark mass. This implies that the bound phase-space volume available for the dark matter at the centre is almost unchanged.

In order to study the effect of baryon outflow on the dark matter, we extend one of our models by removing the satellite. The model concerned is the one with an initially parabolic satellite orbit with $r_{\mathrm{peri}} = 0.4$ falling into a halo with isotropic velocities (blue curves in the right-hand panels of Figs 2 and 3). In Fig. 12, the resulting radial profiles for ρ/σ^3, ρ and ΔM are shown for the situation (i) after satellite accretion (same as the curves in Fig. 3; blue), (ii) further 1000 time units after instant satellite removal (corresponding to a fast wind; magenta) and (iii) after a slow satellite removal (over 250

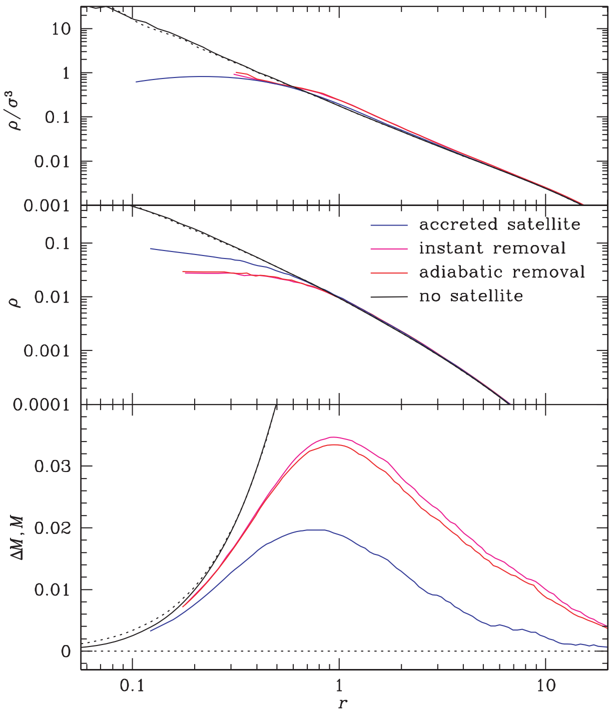

Figure 12. As Fig. 3, but also including the removal of the satellite. The blue curves refer to the same model as the blue curves in Fig. 3. The magenta curves are obtained from this model after instant removal of the satellite, while for the red model the satellite has been slowly removed.

times units followed by another 250 time units without satellite; red). Not surprisingly, the satellite removal has a dramatic effect on the central halo density: the total mass excavated has almost doubled compared to the situation prior to satellite removal and the density has become clearly cored with a central density ∼10 times smaller than the initial density at the radius where initially $m_\mathrm{s} = M(r)$.

The most intriguing plot, however, is that of the pseudo-phase-space density ρ/σ^3 (top panel of Fig. 12). While the redistribution of material to larger radii has shifted the inner profile somewhat, the overall distribution and the maximum value for ρ/σ^3 remained unaffected by the satellite removal. For the slow-wind model this is, of course, expected, since the (true coarse-grained) phase-space density is conserved. Therefore, the additional reduction of ρ and ΔM in this case is entirely owed to the reduction in available phase-space effected by the removal of the satellite potential. Of course, this is a non-linear process because the reduction in central dark matter density itself leads to a further decrease in the potential depth. This explains why the additional mass removed by the satellite departure (the difference between the red/magenta and blue curves) is quite substantial, exceeding the satellite mass.

Somewhat unexpectedly, the fast-wind model is only slightly more efficient at removing dark matter. This strongly suggests that even a fast galactic wind is nearly adiabatic, i.e. has little effect on the (true coarse-grained) phase-space density (which is unaffected by a slow wind).

10 SUMMARY

We have modelled, using *N*-body simulations, the decay of satellite orbits in spherical dark matter halo models with various degrees of velocity anisotropy.

10.1 Orbital evolution

The evolution of the satellite orbits has several phases. First, there is a steady decline in the amplitude of the orbit with almost constant pericentric radius, driven by dynamical friction near pericentre. This is followed by a period of rapid shrinkage of the pericentre coinciding with significant expansion of the innermost halo, as evident from the evolution of the Lagrange radii in Figs 2 and 8.

At this stage the evolution of the halo, driven by the transfer of energy and angular momentum from the decaying satellite orbit, is more or less complete. The time required for this process scales as $t_\mathrm{infall} \propto m_\mathrm{s}^{-0.9}$ with satellite mass, somewhat shallower than the inverse scaling expected from Chandrasekhar's dynamical-friction formula. We also find that t_infall is significantly shorter for decay in haloes with radial velocity anisotropy, because the orbital structure of such haloes makes them more susceptible to perturbations.

The orbital evolution shows some interesting and unexpected behaviour after t_infall. The most bound region of the halo and the satellite form a sort of binary, dominated in mass by the satellite, which is modelled as a single softened particle with size (softening length) $r_\mathrm{s} = 0.03$ (our unit of length is the halo scale radius). Initially, this secondary orbit has amplitude $\approx 0.1 > r_\mathrm{s}$, but after a brief period of apparent growth decays very nearly exponentially with e-folding time of 90 time units.

This is clearly visible in Fig. 13, which plots for all 12 simulations of bound satellite orbits the late time evolution of the distance $|\boldsymbol{x}_\mathrm{s} - \boldsymbol{x}_\mathrm{s}|$ between halo centre and satellite after the initial infall of the satellite. In all these cases the secondary orbital decay occurs. The secondary orbit may be eccentric (as for $r_\mathrm{peri} = 0$ in Fig. 13) or near-circular, when the decay appears more regular. In the case of parabolic satellite orbits (not shown), the secondary decay does not always occur or is much more noisy and less regular.

We are not sure about the cause and dynamics of this phenomenon, and whether it is a numerical artefact or not. It may be related to the form of the softened satellite potential, though the secondary orbital amplitude decays from $\sim 0.2 > r_\mathrm{s}$ to $\sim 0.007 < r_\mathrm{s}$, such that the harmonic inner parts of the softened potential become relevant only in the late stages.

10.2 Effect on halo

Even though the assumed satellite mass was only 1 per cent of the total halo mass, the damage done to the halo is significant: the inner parts of the halo are substantially reduced in density and phase-space density (as indicated by the behaviour of ρ/σ^3), when the

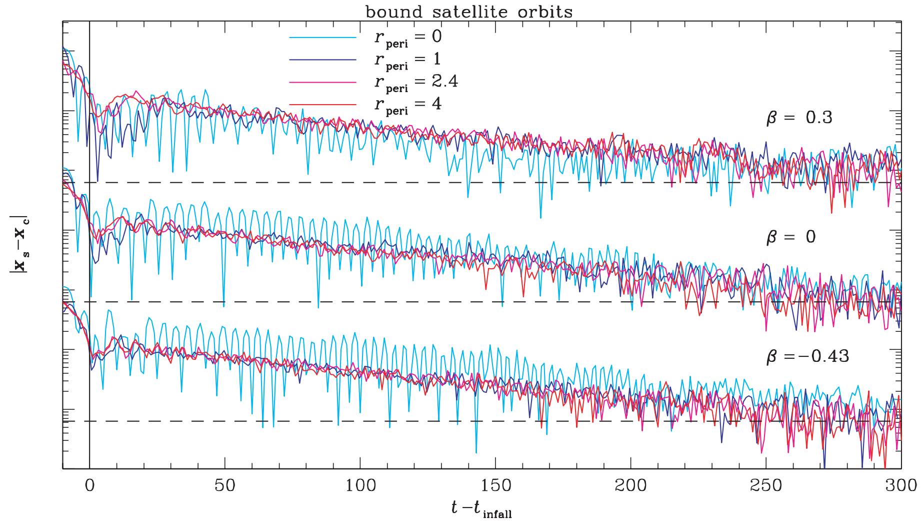

Figure 13. Secondary orbital decay: time evolution of the distance between satellite and halo centre for the 300 time units after the infall time (vertical line) for the bound satellite orbits in halo models with various velocity anisotropy as indicated (the curves for different halo models are offset by 2 dex from each other). The horizontal dashed lines indicate the noise level measured at much later times.

satellite has displaced up to twice its own mass from the innermost halo. The satellite also affects the velocity structure of the inner halo making it more isotropic. Finally, the halo shape becomes triaxial in its inner parts.

We find that the efficiency with which the satellite can affect the halo, e.g. the amount of central density reduction, is increased for haloes with radial velocity anisotropy. This is understandable in terms of the orbital structure of such haloes, making them more vulnerable (see Section 6.1), and relevant, as real dark matter haloes are expected, from simulations of large-scale structure formation, to be radial anisotropic.

One of our most interesting findings is that satellites of smaller mass are relatively more efficient in damaging the halo: the ratio $\Delta M_{\rm max}/m_{\rm s}$ of the maximum displaced halo mass over the satellite mass increases towards smaller satellite masses $m_{\rm s}$ (though the orbital decay time decreases, of course), as in fact predicted by the analytic energy arguments presented in Section 2.

11 DISCUSSION

In this study we have ignored the details of baryonic physics and instead used the simple model of a compact baryonic clump falling into a dark matter halo. Of all possible scenarios for the effect of baryonic physics on the structure of dark matter haloes this is likely the most efficient. This process proved to be highly effective in altering the structure of the dark matter halo in its inner parts, where the galaxy resides. A single clump of only 1 per cent of the total halo mass can reduce the density at $\lesssim 0.1$ halo scale radii by more than an order of magnitude (including the effect of a galactic wind as demonstrated in Section 9), more than sufficient to explain the discrepancies between the rotation curves predicted (using gravity-only simulations) and observed for dark-matter-dominated galaxies (e.g. Simon et al. 2005; de Blok et al. 2008).

The total amount of baryons is one-sixth of all matter (Komatsu et al. 2011), i.e. 0.2 times the dark mass, 20 times more than our model clump. Thus, if the baryonic heating of a dark matter halo is only $\sim$2 per cent efficient on average, the damage done to the halo is equivalent to that in our models, because any additional adiabatic inflow *and* outflow of baryons has no lasting effect on the dark matter.

This assumes, of course, that the baryonic substructures and clumps are able to heat the dark matter particles which contribute to the central cusp. Our simple model of a compact clump, which sinks to the centre of the dark matter halo, is certainly somewhat unrealistic as baryonic structures are susceptible to disruption by tidal forces before they reach the innermost parts of the halo. However, owing to their dissipative nature baryons, unlike dark matter, can form new substructures and clumps, which then continue to heat the dark matter via dynamical friction. Moreover, as our simulations have shown, radial velocity anisotropy, which is typical for dark matter haloes, make their innermost parts more vulnerable to perturbations from the outside. This is because much of the matter in the cuspy region is on eccentric orbits spending most of their time at much larger radii where they are prone to dynamic heating (see also Section 6.1).

11.1 Dark matter contraction versus expansion

A key process in the reshaping of dark matter haloes by non-gravitational baryonic physics is the transfer of energy via dynamical friction from baryonic substructures to the dark matter particles.[5] The effect of this heating can be understood qualitatively by considering the Jeans equation of hydrostatic equilibrium:

$$\nabla(\rho\sigma^2) = -\rho\nabla\Phi. \tag{17}$$

The heating of the dark matter by the non-adiabatic baryon infall raises the central σ^2, which, at fixed ρ, increases the pressure gradient (left-hand side). At the same time, the arrival of the baryons increases the gravitational pull (right-hand side). If these two effects balance exactly, the dark matter density ρ remains unaffected. If the heating dominates, as was the case in our maximally non-adiabatic simulations, then ρ must flatten to retain equilibrium. Conversely, if the gravitational pull dominates (especially for negligible heating, i.e. 'adiabatic contraction'), then ρ has to steepen (and σ^2 will increase adiabatically due to the compression). The exact balance depends on the details and most likely varies systematically with galaxy type, size and environment, explaining the possibility of conflicting results from simulations which attempt to model baryon physics more directly (e.g. Romano-Díaz et al. 2008; Pedrosa et al. 2009).

An alternative way to look at this problem is to consider the effect on the dark matter (coarse-grained) phase-space density, which arguably is dynamically more relevant than the density, because it is conserved for adiabatic evolution. However, the process of baryon infall is inevitably non-adiabatic and reduces the dark matter phase-space density.[6] As long as the accreted baryons remain at the centre, this may not necessarily result in a reduction of the dark matter spatial density, because the additional gravitational potential of the newly arrived baryons increases the available bound velocity space (phase-space at fixed position).

Of course, a galactic wind changes the situation: the loss of some or all of the accreted baryons tips the balance towards a reduction of the dark matter density, as convincingly demonstrated by our models of satellite removal. In the Jeans equation picture the wind removes the additional gravitational pull from the accreted baryons. In the phase-space interpretation, the wind reduces the bound velocity space, thus pressing the dark matter phase-space fluid out of the centre, like toothpaste out of its tube.

11.2 Application to dSph and GCs

For a dwarf spheroidal galaxy our simplistic model of baryon infall may apply even more directly. Given that their present-day baryonic mass is comparable to the dark mass that needs to be rearranged in order to convert their haloes from cusped to cored, it seems plausible that for a reasonable star formation efficiency one could build the stellar component of the dSphs from a number of star clusters that fall to the centre by dynamical friction and in so doing generate a macroscopic core in the halo dark matter distribution of the dSph. For this to work, the clusters need to remain largely unscathed by tides before they reach $\sim 0.1 r_2$. Peñarrubia, Walker & Gilmore (2009) have investigated the tidal disruption of star clusters orbiting in a dSph, in particular the Sagittarius and Fornax satellites to the Milky Way, and used *N*-body simulations to confirm the following

---

[5] While this process itself is, of course, purely gravitational, it is neglected in gravity-only simulations, which ignore the formation of baryonic substructures and unequivocally predict cuspy dark matter haloes.

[6] More precisely, it reduces the excess-mass function:

$$D(f) \equiv \int_{\bar{f}(\boldsymbol{x},\boldsymbol{v})>f} \mathrm{d}\boldsymbol{x}\,\mathrm{d}\boldsymbol{v}\,\left[\bar{f}(\boldsymbol{x},\boldsymbol{v}) - f\right], \tag{18}$$

with $\bar{f}(\boldsymbol{x},\boldsymbol{v})$ the coarse-grained phase-space density (Dehnen 2005).

criterion for the tidal radius $r_{\rm t}$ of a globular cluster (GC) at radius r within a halo:

$$\bar{\rho}_{\rm GC}(r_{\rm t}) \approx 3\,\bar{\rho}_{\rm h}(r). \tag{19}$$

In particular they looked at the resilience of the five GCs in Fornax and found that GCs which retain bound masses of greater than approximately 95 per cent of their total mass do not undergo tidal disruption by the halo. In our simulations the clump falls in to approximately $r = 0.1r_2$ at which point it has excavated the mass in the centre of the halo and reduced the central density. At a corresponding radius in the simulations of (Peñarrubia et al. 2009), four of the GCs are still very stable against tidal disruption. The fifth one is only disrupted when it spends a large fraction of a Hubble time at a radius in the range corresponding to 0.1–0.2r_2 of our model.

In a similar way we can look at the stability of GCs in low surface brightness (LSB) galaxies. Kuzio de Naray, McGaugh & de Blok (2008) and Kuzio de Naray et al. (2006) investigated the density profiles of a number of LSB galaxies and attempted to fit them using NFW and pseudo-isothermal halo models. Their best-fitting NFW models should give an upper limit to the density in the inner halo and therefore the one most likely able to disrupt an infalling object. Using these we find a range of values for $\bar{\rho}_{\rm h}(r)$ at 0.1 scale radii ranging from 0.012 to 0.080 $\mathrm{M_\odot\,pc^{-3}}$. These are lower than the corresponding value for Fornax which is $\sim$0.13 $\mathrm{M_\odot\,pc^{-3}}$. Based on the work of Peñarrubia et al. (2009) this implies that GCs would also be stable at $0.1r_2$ in LSB galaxies.

ACKNOWLEDGMENTS

Research in Theoretical Astrophysics at Leicester is supported by a STFC rolling grant. MIW acknowledges the Royal Society for support through a University Research Fellowship. We thank James Binney, Scott Tremaine and Justin Read for useful discussions. This research used the ALICE High Performance Computing Facility at the University of Leicester. Some resources on ALICE form part of the DiRAC Facility jointly funded by STFC and the Large Facilities Capital Fund of BIS.

REFERENCES

Arena S. E., Bertin G., 2007, A&A, 463, 921
Athanassoula E., 2002, ApJ, 569, L83
Athanassoula E., 2003, MNRAS, 341, 1179
Binney J. J., Tremaine S., 2008, Galactic Dynamics, 2nd edn. Princeton Univ. Press, Princeton, NJ
Blumenthal G. R., Faber S. M., Flores R., Primack J. R., 1986, ApJ, 301, 27
Chandrasekhar S., 1943, ApJ, 97, 255
Cuddeford P., 1991, MNRAS, 253, 414
de Blok W. J. G., 2010, Adv. Astron., 2010, 5
de Blok W. J. G., Walter F., Brinks E., Trachternach C., Oh S., Kennicutt R. C., 2008, AJ, 136, 2648
Dehnen W., 2002, J. Comput. Phys., 179, 27
Dehnen W., 2005, MNRAS, 360, 892
Dehnen W., 2009, MNRAS, 395, 1079
Dehnen W., McLaughlin D. E., 2005, MNRAS, 363, 1057
Dubinski J., Carlberg R. G., 1991, ApJ, 378, 496
Einasto J., Einasto L., 1972, Tartu Astrofuusika Obser. Teated, 36, 3
El-Zant A., Shlosman I., Hoffman Y., 2001, ApJ, 560, 636
El-Zant A. A., Hoffman Y., Primack J., Combes F., Shlosman I., 2004, ApJ, 607, L75
Gilmore G., Wilkinson M. I., Wyse R. F. G., Kleyna J. T., Koch A., Evans M. W., Grebel E. K., 2007, ApJ, 663, 948
Gnedin O. Y., Zhao H., 2002, MNRAS, 333, 299
Gnedin O. Y., Kravtsov A. V., Klypin A. A., Nagai D., 2004, ApJ, 616, 16
Goerdt T., Moore B., Read J. I., Stadel J., Zemp M., 2006, MNRAS, 368, 1073
Goerdt T., Moore B., Read J. I., Stadel J., 2010, ApJ, 725, 1707
Hansen S. H., Moore B., 2006, New Astron., 11, 333
Jardel J. R., Sellwood J. A., 2009, ApJ, 691, 1300
Johansson P. H., Naab T., Ostriker J. P., 2009, ApJ, 697, L38
Komatsu E. et al., 2011, ApJ, 192, 18
Kuzio de Naray R., McGaugh S. S., de Blok W. J. G., Bosma A., 2006, ApJS, 165, 461
Kuzio de Naray R., McGaugh S. S., de Blok W. J. G., 2008, ApJ, 676, 920
Navarro J. F., Frenk C. S., White S. D. M., 1995, MNRAS, 275, 720
Navarro J. F., Frenk C. S., White S. D. M., 1997, ApJ, 490, 493
Navarro J. F. et al., 2004, MNRAS, 349, 1039
Navarro J. F. et al., 2010, MNRAS, 402, 21
Nipoti C., Treu T., Ciotti L., Stiavelli M., 2004, MNRAS, 355, 1119
Pedrosa S., Tissera P. B., Scannapieco C., 2009, MNRAS, 395, L57
Peñarrubia J., Walker M. G., Gilmore G., 2009, MNRAS, 399, 1275
Read J. I., Gilmore G., 2005, MNRAS, 356, 107
Read J. I., Goerdt T., Moore B., Pontzen A. P., Stadel J., Lake G., 2006, MNRAS, 373, 1451
Romano-Díaz E., Shlosman I., Hoffman Y., Heller C., 2008, ApJ, 685, L105
Simon J. D., Bolatto A. D., Leroy A., Blitz L., Gates E. L., 2005, ApJ, 621, 757
Spano M., Marcelin M., Amram P., Carignan C., Epinat B., Hernandez O., 2008, MNRAS, 383, 297
Springel V., Frenk C. S., White S. D. M., 2006, Nat, 440, 1137
Tremaine S., Henon M., Lynden Bell D., 1986, MNRAS, 219, 285
Warren M. S., Quinn P. J., Salmon J. K., Zurek W. H., 1992, ApJ, 399, 405
Weinberg M. D., Katz N., 2002, ApJ, 580, 627

This paper has been typeset from a TEX/LATEX file prepared by the author.